An efficient SPH framework for modelling binary granular mixtures and implications for granular flows

Shuaihao Zhang[a], Dong Wu[b], Xiangyu Hu[b], Clarence E. Choi[a], Sérgio D.N. Lourenço[a,*]

[a]*Department of Civil Engineering, The University of Hong Kong, Pokfulam, Hong Kong SAR, China*
[b]*School of Engineering and Design, Technical University of Munich, 85748 Garching, Germany*

Abstract

A two-way coupling numerical framework based on smoothed particle hydrodynamics (SPH) is developed in this study to model binary granular mixtures consisting of coarse and fine grains. The framework employs updated Lagrangian SPH to simulate fine grains, with particle configurations updated at each time step, and total Lagrangian SPH to efficiently model coarse grains without updated particle configurations. A Riemann solver is utilized to introduce numerical dissipation in fine grains and facilitate their coupling with coarse grains. To enhance computational efficiency, a multiple time-stepping scheme is initially applied to manage the time integration coupling between coarse and fine grains. Several numerical experiments, including granular column collapse, low-speed impact craters, and granular flow impacting blocks, are conducted to validate the stability and accuracy of the proposed algorithm. Subsequently, two more complex scenarios involving a soil-rock mixture slope considering irregular coarse particle shapes, and bouldery debris flows on natural terrain, are simulated to showcase the potential engineering applications. Finally, a detailed analysis is performed to evaluate the computational efficiency advantages of the present approach. The findings of this study are consistent with previous experimental and numerical results, and the implementation of a multiple time-stepping scheme can improve computational efficiency by up to 600%, thereby providing significant advantages for large-scale engineering simulations.

Keywords: Smoothed particle hydrodynamics; Granular materials; Binary mixtures; Bouldery debris flow; Updated Lagrangian formulation

1. Introduction

Binary mixtures are granular materials made up of both coarse and fine grains [1]. In geotechnical engineering, earth sciences, geological engineering, and mining engineering, binary mixtures are commonly encountered materials, such as soil-rock mixtures (SRM) in natural slopes [2], boulders mixed with soils in debris flows [3], gravel-sand mixtures in dam filling [4], ballast-fouling mixtures in railway track beds [5], and mining waste rock and tailing [6].

*Corresponding author.
Email address: lourenco@hku.hk (Sérgio D.N. Lourenço)

Discrete element method (DEM) [7] is widely used to model granular mixtures [1, 8], where fine grains and coarse grains are represented by discrete particles of different sizes. However, DEM requires solving for each discrete particle individually, resulting in significant computational time and memory overhead [9, 10]. Some researchers used a continuum model, which only captures the macroscopic information of the material such as stress and strain, to simulate fine grains. This is then coupled with DEM-simulated coarse grains to improve computational efficiency. Coupling the finite element method (FEM) with DEM to simulate granular mixtures is one of such approaches [11, 12]. However, when the material undergoes large and nonuniform deformations, translations, or rotations, the mesh in FEM can become ill-shaped [9], affecting its computational accuracy. Therefore, some continuum methods suited for large deformations, such as the material point method (MPM), have also been used to model fine grains and coupled with DEM [13, 14, 15].

Smoothed particle hydrodynamics (SPH) [16, 17] has become a popular method in recent years for simulating large deformations of granular materials [18, 19, 20, 21]. Unlike MPM, SPH is a fully particle-based mesh-free method where all physical quantities, such as density, velocity, and stress, are carried by particles and updated through interactions between each particle and those within its support domain. Due to its mesh-free nature, the SPH method facilitates efficient modeling of granular flows with substantial strains and displacements [9]. SPH methods can be classified into total Lagrangian SPH (TLSPH) [22, 23] and updated Lagrangian SPH (ULSPH) [24, 25] based on whether the particle configurations, which define each particle's neighbors, are updated during the simulation. TLSPH and ULSPH each have distinct characteristics that make them suitable for different applications. TLSPH is efficient in handling elastic and plastic dynamics as it avoids the computational cost of continuously updating particle configurations, while ULSPH, by updating particle configurations at each time step, is better suited for modeling material failure and fracture beyond elastic or plastic deformations [26].

Over the past 30 years, the SPH method has evolved and been successfully applied to simulate fluid dynamics [27], solids [24], and fluid-structure interactions [28, 29]. Bui et al. [18] firstly applied the ULSPH method to simulate large deformations of granular materials and validated the numerical model with experimental results. Since then, this approach has been widely used for simulating elastoplastic granular materials [25, 30, 31, 32, 33, 34, 35]. Based on this, Hu et al. [9] developed a coupling algorithm that uses ULSPH to simulate fine grains as granular materials, which is then coupled with moving solid bodies. Peng et al. [36] simulated the interaction between non-Newtonian fluids and solid particles with the SPH-DEM coupling method.

In this study, the simulation of binary granular mixtures is implemented within a unified SPH framework. Fine grains, such as clay and silt in debris flows, exhibit highly dynamic and irregular motion and displacement, with constantly changing particle configurations (neighboring particles), necessitating the use of ULSPH for accurate simulation [18] as elasto-plastic materials. In contrast, the particle configuration of each coarse grain, assuming no breakage, keeps unchanged [26]. This feature allows TLSPH to simulate each coarse grain as an elastic body (Neo-Hookean materials in this study), enhancing computational efficiency [22]. Building on Zhang et al.'s study [20], a Riemann solver is introduced to replace artificial viscosity [37, 18] in modeling fine grains, aiming to reduce numerical dissipation while maintaining high accuracy. The stress diffusion term [38] is also applied in fine grain modeling to eliminate spurious stress profiles and achieve a smooth stress

distribution. Additionally, a multiple time-stepping scheme, originally proposed for fluid-structure interactions [39], is introduced in modelling granular materials for the first time to handle coupled time integration for coarse and fine grains, significantly enhancing computational efficiency. The irregular shape of coarse particles can be incorporated by utilizing level-set based pre-processing techniques [40]. Compared to previous methods that use DEM [1, 8], FEM-DEM [11, 12], MPM-DEM [14, 15], or SPH-DEM [36] to simulate binary granular mixtures, the approach in this study offers the following advantages: (1) it delivers a two-way coupling between fine and coarse grains within a unified SPH framework; (2) SPH is a mesh-free method that effectively handles large deformations in granular flows; (3) compared to DEM, SPH is a continuum method that offers higher computational efficiency.

The remainder of this paper is arranged as follows. Sections 2 and 3 introduce the theories behind ULSPH-based fine grain modeling and TLSPH-based coarse grain modeling, respectively. Section 4 presents the ULSPH-TLSPH coupling method for simulating binary granular mixtures. Section 5 validates the stability and accuracy of the proposed numerical method through several commonly used test cases. In Section 6, two more complex cases are used to demonstrate the potential engineering applications of the algorithm. Section 7 analyzes the computational efficiency of the method, and Section 8 provides the conclusion.

2. ULSPH for modelling fine grains

ULSPH is used to simulate fine grains, with updating particle configurations at each time step. Note that the term 'fine' is used throughout this paper as the opposite of 'coarse'. It does not refer to soil grains smaller than 0.075 mm [1, 41]. In SPH, each particle represents a continuous finite volume. This study considers the size of fine grains to be the size of the continuous region represented by each SPH particle [9], specifically the initial particle spacing dp. The actual physical size of these fine grains is not constrained; it can range from a few millimeters when simulating small-scale problems [18] to several meters for large-scale problems [42]. The size of each coarse grain is determined by the outline formed by multiple SPH particles, as shown in Fig. 1. In the present method, there is no upper limit on the size of coarse grains. However, based on previous studies where the wall-boundary condition involved three or four layers of particles [18, 20, 43], the minimum size is set to four times that of the fine grains. A coarse grain of this size is capable of accurately representing its shape after discretization. As shown in Fig. 1, coarse particle-1 is an example, with its size being approximately four times that of the fine grains.

2.1. Governing equations and constitutive model

For the updated Lagrangian framework, the motion state is described based on the current configuration. The governing equations in ULSPH, including the conservation of mass and momentum, are defined as

$$\frac{\mathrm{d}\rho}{\mathrm{d}t} = -\rho\nabla\cdot\mathbf{v} \tag{1}$$

$$\frac{\mathrm{d}\mathbf{v}}{\mathrm{d}t} = \frac{1}{\rho}\nabla\cdot\boldsymbol{\sigma} + \mathbf{g} + \frac{1}{m}\mathbf{f}^{c\to f} \tag{2}$$

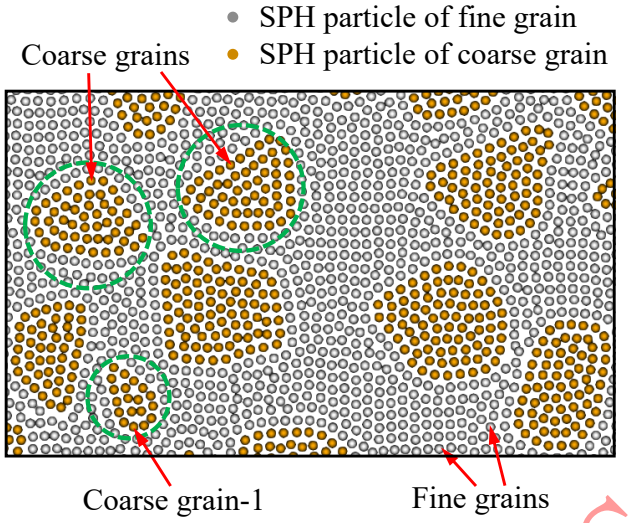

Fig. 1. A binary mixture of coarse and fine grains implemented with SPH.

where ρ is the density, $\mathbf{v}$ is velocity, $\mathbf{g}$ is the body force. ∇ is the gradient operator and $\frac{\mathrm{d}}{\mathrm{d}t}$ donates the material derivative. m is the particle mass, and $\mathbf{f}^{c\to f}$ represents the force exerted by coarse grains on fine grains. $\boldsymbol{\sigma}$ is the stress tensor (negative for compression) and can be calculated by integrating the stress rate $\dot{\boldsymbol{\sigma}}$ with respect to time.

$$\boldsymbol{\sigma} = \int_0^t \dot{\boldsymbol{\sigma}} \mathrm{d}t \tag{3}$$

The elastic-perfectly plastic Drucker-Prager constitutive model with non-associated flow rule [44, 45] is adopted here to describe the stress-strain relationship of granular materials with fine grains. The yield criterion f and plastic potential function g are defined as [44, 45]

$$f(I_1, J_2) = \alpha_\phi I_1 + \sqrt{J_2} - k_c \tag{4}$$

$$g(I_1, J_2) = \alpha_\psi I_1 + \sqrt{J_2} \tag{5}$$

where $I_1 = \mathrm{tr}(\boldsymbol{\sigma})$ and $J_2 = \frac{1}{2}\boldsymbol{\sigma}^s : \boldsymbol{\sigma}^s$ are the first and second invariant of stress tensor, respectively. The symbol : represents the double contraction of tensors. α_ϕ, k_c and α_ψ are material constants, and are defined as [45, 46, 47, 48]

$$\alpha_\phi = \frac{\tan\phi}{\sqrt{9 + 12\tan^2\phi}}, k_c = \frac{3c}{\sqrt{9 + 12\tan^2\phi}}, \alpha_\psi = \frac{\tan\psi}{\sqrt{9 + 12\tan^2\psi}} \tag{6}$$

Here, c is cohesion, ϕ is friction angle, and ψ is dilation angle. The Jaumann stress rate that is invariant to rigid-body rotation for Drucker-Prager model with non-associated flow rule can be expressed as [45]

$$\dot{\boldsymbol{\sigma}} = 2G\dot{\boldsymbol{\varepsilon}} + K\mathrm{tr}(\dot{\boldsymbol{\varepsilon}})\mathbf{I} - \dot{\gamma}\left(3K\alpha_\phi \mathbf{I} + \frac{G}{\sqrt{J_2}}\boldsymbol{\sigma}^s\right) + \boldsymbol{\sigma}\cdot\dot{\boldsymbol{\omega}}^T + \dot{\boldsymbol{\omega}}\cdot\boldsymbol{\sigma} \tag{7}$$

where $\boldsymbol{\sigma}^s = \boldsymbol{\sigma} - \frac{1}{3}\text{tr}(\boldsymbol{\sigma})\mathbf{I}$ is the deviatoric stress tensor. The last two terms $\boldsymbol{\sigma}\cdot\dot{\boldsymbol{\omega}}^T + \dot{\boldsymbol{\omega}}\cdot\boldsymbol{\sigma}$ are introduced to mitigate the influence of rigid rotation, with the superscript T being the transpose of a tensor. G and K are the elastic shear modulus and bulk modulus. $\boldsymbol{\omega}$ is the spin tensor and $\mathbf{I}$ is the identity matrix. γ is the plastic multiplier, and $\gamma = 0$ if $f < 0$ or $f = 0$ & $df < 0$ corresponds to elastic behavior or plastic unloading, while $\gamma > 0$ if $f = 0$ & $df = 0$ corresponds plastic loading. The Jaumann stress rate is widely used in SPH literature [18, 33, 38]; however, it is prone to oscillations under simple shear [49], as also noted by Castillo et al. [32]. Nevertheless, their study [32] further shows that even when applying the Jaumann stress rate in SPH simulations, these oscillations were not observed in both simple shear and large deformation problems, partly due to the very small time steps employed in explicit time integration. Nonetheless, other objective stress rates, such as those based on the Lie derivative [50], could also be used here. For non-associated flow rule, $\dot{\gamma}$ is defined as [45, 51]

$$\dot{\gamma} = \frac{3\alpha_\phi K\text{tr}(\dot{\boldsymbol{\varepsilon}}) + (G/\sqrt{J_2})\boldsymbol{\sigma}^s : \dot{\boldsymbol{\varepsilon}}}{9\alpha_\phi K\alpha_\psi + G} \tag{8}$$

$\dot{\boldsymbol{\varepsilon}}$ and $\dot{\boldsymbol{\omega}}$ are strain rate and spin rate, respectively.

$$\dot{\boldsymbol{\varepsilon}} = \frac{1}{2}\left[\nabla\boldsymbol{v} + (\nabla\boldsymbol{v})^T\right] \tag{9}$$

$$\dot{\boldsymbol{\omega}} = \frac{1}{2}\left[\nabla\boldsymbol{v} - (\nabla\boldsymbol{v})^T\right] \tag{10}$$

The integration of the constitutive model employs the two-step elastic predictor-plastic corrector scheme, also known as return mapping algorithms [45, 52]. In this scheme, an initial elastic trial solution is computed by integrating the constitutive equations with the strain increment. The resulting stress is then evaluated against the yield function. If the stress falls within or on the yield surface, the trial solution is accepted. However, if the stress lies outside the yield surface, the plastic corrector step is iteratively performed to bring the trial stress back to the yield surface [18, 34]. When condition $-\alpha_\phi I_1 + k_c < 0$ is met, the hydrostatic stress component can be adjusted by

$$\widetilde{\boldsymbol{\sigma}} = \boldsymbol{\sigma} - \frac{1}{3}\left(I_1 - \frac{k_c}{\alpha_\phi}\right)\mathbf{I} \tag{11}$$

When condition $-\alpha_\phi I_1 + k_c < \sqrt{J_2}$ is satisfied, the deviatoric stress component can be adjusted by

$$\widetilde{\boldsymbol{\sigma}} = \frac{-\alpha_\phi I_1 + k_c}{\sqrt{J_2}}\boldsymbol{\sigma}^s + \frac{1}{3}I_1\mathbf{I} \tag{12}$$

where the $\boldsymbol{\sigma}$ and $\widetilde{\boldsymbol{\sigma}}$ are the stress before and after return mapping.

2.2. SPH discretization

The prevalent SPH discretization approach [24, 38] for the governing Eqs. (1) and (2) is

$$\frac{\mathrm{d}\rho_i}{\mathrm{d}t} = \rho_i\sum_j \mathbf{v}_{ij}\cdot\nabla_i W_{ij}V_j \tag{13}$$

$$\frac{\mathrm{d}\mathbf{v}_i}{\mathrm{d}t} = \frac{1}{\rho_i}\sum_j \left(\boldsymbol{\sigma}_i + \boldsymbol{\sigma}_j\right)\cdot\nabla_i W_{ij} V_j + \mathbf{g} + \frac{1}{m_i}\mathbf{f}_i^{c\to f} \tag{14}$$

where W_{ij} represents $W(\mathbf{r}_i - \mathbf{r}_j, h)$, which is the kernel function, and $\nabla_i W_{ij} = \frac{\partial W_{ij}}{\partial r_{ij}}\mathbf{e}_{ij} = \frac{\partial W(|\mathbf{r}_{ij}|,h)}{\partial |\mathbf{r}_{ij}|}\mathbf{e}_{ij}$. $\mathbf{r}_{ij} = |\mathbf{r}_i - \mathbf{r}_j|$ is the distance between two particles, with $\mathbf{r}$ being the particle position and h being the smoothing length. $\mathbf{e}_{ij}$ is the unit vector pointing from particle j to particle i and $\mathbf{v}_{ij} = \mathbf{v}_i - \mathbf{v}_j$. The subscripts i and j donate particle numbers, and V is the particle volume. $\mathbf{f}_i^{c\to f}$ will be calculated in Section 4.1.

Rather than using artificial viscosity [18, 38, 37], which introduces the numerical dissipation explicitly, we utilize a low-dissipation Riemann solver [20, 53] to introduce numerical dissipation implicitly. The discrete form of the governing equations after introducing the Riemann problem is shown as Eqs. (15) and (16). The detailed derivation process can be found in reference [20, 53].

$$\frac{\mathrm{d}\rho_i}{\mathrm{d}t} = 2\rho_i \sum_j (\mathbf{v}_i - \mathbf{v}^*)\cdot\nabla_i W_{ij} V_j \tag{15}$$

$$\frac{\mathrm{d}\mathbf{v}_i}{\mathrm{d}t} = 2\frac{1}{\rho_i}\sum_j \boldsymbol{\sigma}^*\cdot\nabla_i W_{ij} V_j + \mathbf{g} + \frac{1}{m_i}\mathbf{f}_i^{c\to f} \tag{16}$$

The Riemann solutions $\mathbf{v}^*$, $\boldsymbol{\sigma}^*$ are expressed as

$$\mathbf{v}^* = U^*\mathbf{e}_{ij} + \left(\overline{\mathbf{v}}_{ij} - \overline{U}\mathbf{e}_{ij}\right) \tag{17}$$

$$\boldsymbol{\sigma}^* = \overline{\boldsymbol{\sigma}}_{ij}^s - P^*\mathbf{I} \tag{18}$$

Here, $\overline{U} = (U_L + U_R)/2$. $\overline{\mathbf{v}}_{ij} = (\mathbf{v}_i + \mathbf{v}_j)/2$ and $\overline{\boldsymbol{\sigma}}_{ij}^s = (\boldsymbol{\sigma}_i^s + \boldsymbol{\sigma}_j^s)/2$ are the particle-average velocity and shear stress between particles i and j, respectively. U^* and P^*, which are obtained from the low-dissipation Riemann solver [53, 20, 26], are the solutions of an inter-particle Riemann problem.

$$U^* = \frac{\rho_L c_L U_L + \rho_R c_R U_R + P_L - P_R}{\rho_L c_L + \rho_R c_R} \tag{19}$$

$$P^* = \frac{\rho_L c_L P_R + \rho_R c_R P_L + \beta\rho_L c_L \rho_R c_R (U_L - U_R)}{\rho_L c_L + \rho_R c_R} \tag{20}$$

The subscripts L and R denote the left and right states obtained from the Riemann problem, and are defined as

$$\begin{cases} (\rho_L, U_L, P_L, c_L) = (\rho_i, \mathbf{v}_i\cdot\mathbf{e}_{ij}, P_i, c_{0i}) \\ (\rho_R, U_R, P_R, c_R) = (\rho_j, \mathbf{v}_j\cdot\mathbf{e}_{ij}, P_j, c_{0j}) \end{cases} \tag{21}$$

where $P_i = -\frac{1}{3}\mathrm{tr}(\boldsymbol{\sigma}_i)$. c_0 is the speed of sound and is defined as [26]

$$c_0 = \sqrt{\frac{E}{3(1-2\nu)\rho_0}} \tag{22}$$

where E is the Young's modulus, ν is the Poisson's ratio, and ρ_0 is the initial density. β in Eq. (20) is a dissipation limiter, and is expressed as [53]

$$\beta = \min\left\{\eta \max\left[\frac{(P_L + P_R)(U_L - U_R)}{\rho_L c_L + \rho_R c_R}, 0\right], 1.0\right\} \tag{23}$$

η is a coefficient that controls the numerical dissipation, and is set $20d$ [20] in this study unless otherwise specified, with d donating the space dimension. The velocity gradient $\nabla \mathbf{v}$ in Eqs. (9) and (10) can be discretized as

$$\nabla \mathbf{v} = \sum_j \mathbf{v}_{ij} \otimes \nabla_i W_{ij} V_j \tag{24}$$

To achieve a smooth stress distribution, a stress diffusion term [38] is incorporated into the constitutive equation by adding another term $\boldsymbol{D}$ in the right-hand side of Eq. (7). For a particle i, the stress diffusion term $\boldsymbol{D}_i$ is defined as

$$\boldsymbol{D}_i = 2\zeta h c_0 \sum_j \boldsymbol{\Psi}_{ij} \frac{\mathbf{r}_{ij}}{|\mathbf{r}_{ij}|^2 + 0.01h^2} \nabla_i W_{ij} V_j \tag{25}$$

The coefficient ζ is introduced to regulate the magnitude of the diffusion term and is set to 0.1 [38]. If the direction of the z-coordinate axis is opposite to the direction of gravity $\mathbf{g}$, the diffusion operator $\boldsymbol{\Psi}_{ij}$ can be defined as

$$\begin{cases} \Psi_{ij}^{\alpha\beta} = \sigma_{ij}^{\alpha\beta} & \alpha \neq \beta \\ \Psi_{ij}^{xx} = \sigma_{ij}^{xx} - K_0 \rho_0 |\mathbf{g}| z_{ij} \\ \Psi_{ij}^{yy} = \sigma_{ij}^{yy} - K_0 \rho_0 |\mathbf{g}| z_{ij} \\ \Psi_{ij}^{zz} = \sigma_{ij}^{zz} - \rho_0 |\mathbf{g}| z_{ij} \end{cases} \tag{26}$$

where $z_{ij} = z_i - z_j$ is the distance between two particles along z-axis. $K_0 = 1 - sin(\phi)$ is Jaky's earth pressure coefficient at rest.

2.3. Tensile instability

If the granular material is cohesive, the well-known issue of tensile instability [24] will arise during SPH simulations, manifesting as particle clustering and non-physical fractures. This problem does not occur in non-cohesive granular materials because tensile instability only appears in regions under tension, and non-cohesive granular materials cannot sustain tensile stress. Gray et al. proposed an artificial stress term to address tensile instability [24], which was later incorporated into the simulation of cohesive granular materials by Bui et al. [18]. Specifically, an additional artificial stress term $\mathbf{R}$, acting as a repulsive force, was introduced into the momentum equation. This repulsive force increases as the distance between particles decreases, thereby preventing particle clustering. The momentum equation Eq. (16) with the introduced artificial stress term is rewritten as

$$\frac{\mathrm{d}\mathbf{v}_i}{\mathrm{d}t} = 2\frac{1}{\rho_i} \sum_j \left(\boldsymbol{\sigma}^* + f_{ij}^n \overline{\mathbf{R}}_{ij}\right) \cdot \nabla_i W_{ij} V_j + \mathbf{g} + \frac{1}{m_i} \mathbf{f}_i^{c \to f} \tag{27}$$

where $\overline{\mathbf{R}}_{ij} = (\mathbf{R}_i + \mathbf{R}_j)/2$. $f_{ij} = W(|\mathbf{r}_{ij}|, h)/W(dp, h)$ is a coefficient which increases with reducing particle distance $|\mathbf{r}_{ij}|$. The exponent n is set to 2.55, based on the value used by Bui et al. [18] for granular materials.

The fundamental procedure of artificial stress involves first diagonalizing the stress tensor by means of a coordinate system rotation. Subsequently, an additional artificial stress term is added to each positive component (tension) of the diagonalized stress tensor. Finally, the value of the artificial stress in the original coordinate system is determined by rotating the coordinate system back. In two dimensions, each component of the second-order tensor $\mathbf{R_i}$ is defined by [24]

$$\begin{cases} R_i^{xx} = \cos^2\theta_i R_i^{'xx} + \sin^2\theta_i R_i^{'yy} \\ R_i^{yy} = \sin^2\theta_i R_i^{'xx} + \cos^2\theta_i R_i^{'yy} \\ R_i^{xy} = \sin\theta_i \cos\theta_i (R_i^{'xx} - R_i^{'yy}) \end{cases} \tag{28}$$

where $R_i^{'xx}$ and $R_i^{'yy}$ are the principal stress components. θ_i is the rotation angle of the coordinate system when diagonalizing the stress tensor, and is given by [24]

$$\tan 2\theta_i = \frac{2\sigma_i^{xy}}{\sigma_i^{xx} - \sigma_i^{yy}} \tag{29}$$

Here, σ_i^{xx}, σ_i^{yy}, and σ_i^{xy} are the components of the stress tensor in the original coordinate system. The diagonal components of the artificial stress term is calculated by [24]

$$R_i^{'xx} = \begin{cases} -\epsilon \dfrac{\sigma_i^{'xx}}{\rho_i^2} & \text{if} \quad \sigma_i^{'xx} > 0 \\ 0 & \text{if} \quad \sigma_i^{'xx} \le 0 \end{cases} \tag{30}$$

The parameter ϵ is a positive constant, and is set to 0.5 for granular materials according to Bui et al. [18]. The diagonal components of stress tensor $\sigma_i^{'xx}$ and $\sigma_i^{'yy}$ are obtained by [24]

$$\begin{cases} \sigma_i^{'xx} = \cos^2\theta_i \sigma_i^{xx} + 2\sin\theta_i \cos\theta_i \sigma_i^{xy} + \sin^2\theta_i \sigma_i^{yy} \\ \sigma_i^{'yy} = \sin^2\theta_i \sigma_i^{xx} + 2\sin\theta_i \cos\theta_i \sigma_i^{xy} + \cos^2\theta_i \sigma_i^{yy} \end{cases} \tag{31}$$

The extension of the aforementioned methods to three-dimensional (3D) problems is quite complicated, primarily due to the intricate and time-consuming process of diagonalizing matrices through coordinate rotation in 3D scenarios. A more simplified approach known as artificial pressure [54] is typically employed for 3D cases. In this study, only one two-dimensional (2D) example involves cohesive granular material (as shown in Section 6.1), which exhibits tensile instability; therefore, the method proposed by Gray et al. [24] is adopted.

2.4. Wall-boundary condition

As shown in Fig. 2, four layers of fixed dummy particles are used to impose the wall-boundary condition [43]. Real particles represent the particles for simulated materials, specifically referring to fine grains here.

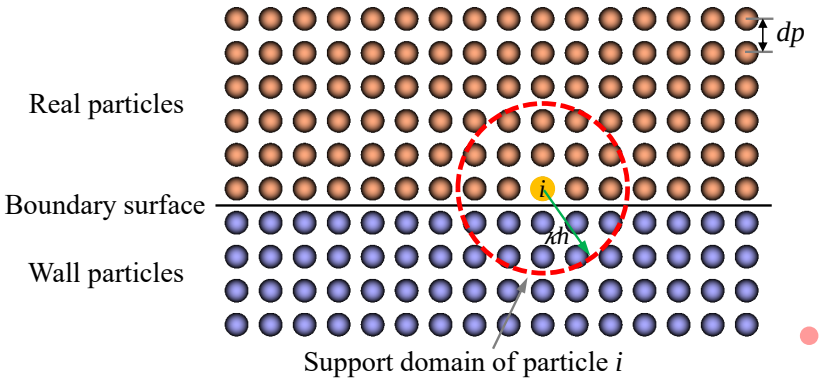

Fig. 2. Illustration of the wall-boundary condition. Here, dp represents the initial particle spacing. The smoothing length $h = 1.3dp$ and the cut-off radius $\kappa h = 2.6dp$

By solving a one-sided Riemann problem [53] along the wall's normal direction, the interaction between real particles and wall particles is determined. When dealing with real particle i, if wall particles are present within the support domain of particle i, the stress of the wall particles can be set to be equal to the stress of the real particle i, i.e., $\boldsymbol{\sigma}_w = \boldsymbol{\sigma}_i$ to achieve a non-slip boundary condition [18]. In this specific Riemann problem, the left state is defined as

$$(\rho_L, U_L, P_L, c_L) = (\rho_f, -\mathbf{n}_w \cdot \mathbf{v}_f, P_f, c_{0f}) \tag{32}$$

where the subscript f represents the SPH particles for fine grains and w represents wall particles. $\mathbf{n}_w$ is the local wall norm direction and is defined as [53]

$$\mathbf{n}_w = \frac{\boldsymbol{\Phi}(\mathbf{r}_i)}{|\boldsymbol{\Phi}(\mathbf{r}_i)|}, \quad \boldsymbol{\Phi}(\mathbf{r}_i) = -\sum_{j \in w} \nabla_i W_{ij} V_j \tag{33}$$

The summation in Eq. (33) is restricted to wall particles only. Based on the physical wall boundary condition, the right-state velocity U_R is defined as [53]

$$U_R = -U_L + 2u_W \tag{34}$$

where u_W is the prescribed wall velocity. The right-state pressure is assumed as [53]

$$P_R = P_L + \rho_f \mathbf{g} \cdot \mathbf{r}_{fw} \tag{35}$$

where $\mathbf{r}_{fw} = \mathbf{r}_f - \mathbf{r}_w$.

3. TLSPH for modelling coarse grains

TLSPH is employed to simulate the finite deformations of coarse grains, enhancing computational efficiency by bypassing the need to update particle configurations.

3.1. Governing equations and constitutive model

The kinematics can be characterized by introducing a deformation map, denoted as φ, which describes the mapping of a material point $\mathbf{r}^0$ from the initial reference configuration $\Omega^0 \in \mathbb{R}^d$ to the corresponding point $\mathbf{r} = \varphi(\mathbf{r}^0, t)$ in the deformed configuration $\Omega = \varphi(\Omega^0)$. In this study, the superscript $(\bullet)^0$ represents the quantities in the initial reference configuration. The deformation tensor $\mathbb{F}$ can be defined as the gradient of the current position with respect to the initial reference configuration, expressed as

$$\mathbb{F} = \frac{\partial \mathbf{r}}{\partial \mathbf{r}^0} = \nabla^0 \mathbf{u} + \mathbf{I} \tag{36}$$

where $\mathbf{u} = \mathbf{r} - \mathbf{r}^0$ is the displacement, and ∇^0 is the spatial gradient operator with respect to the initial reference configuration. In the total Lagrangian formulation, the conservation equations for mass and momentum can be formulated as

$$\rho = J^{-1}\rho^0 \tag{37}$$

$$\frac{\mathrm{d}\mathbf{v}}{\mathrm{d}t} = \frac{1}{\rho^0}\nabla^0 \cdot \mathbb{P}^T + \mathbf{g} + \frac{1}{m}\mathbf{f}^{f\to c} \tag{38}$$

where $J = \det(\mathbb{F})$ is the determinant of the deformation tensor. ρ^0 and ρ are the initial and current densities, respectively. $\mathbb{P} = \mathbb{F}\mathbb{S}$ is the first Piola-Kirchhoff stress tensor, with $\mathbb{S}$ denoting the second Piola-Kirchhoff stress tensor. $\mathbf{f}^{f\to c}$ represents the force exerted by fine grains on coarse grains.

In this study, the coarse grains are modelled with Neo-Hookean materials, which can be defined in general form by introducing the strain-energy density function [55]

$$\mathbb{W} = \mu \mathrm{tr}(\mathbb{E}) - \mu \ln J + \frac{\lambda}{2}(\ln J)^2 \tag{39}$$

The second Piola-Kirchhoff stress tensor for the Neo-Hookean model is defined as [55]

$$\mathbb{S} = \frac{\partial \mathbb{W}}{\partial \mathbb{E}} = \mu(\mathbf{I} - \mathbb{C}^{-1}) + \lambda(\ln J)\mathbb{C}^{-1} \tag{40}$$

where λ and μ are the Lamé parameters, with $K = \lambda + 2\mu/3$ and $G = \mu$. $\mathbb{E}$ is the Green-Lagrangian strain tensor and is defined as

$$\mathbb{E} = \frac{1}{2}\left(\mathbb{F}^T\mathbb{F} - \mathbf{I}\right) = \frac{1}{2}(\mathbb{C} - \mathbf{I}) \tag{41}$$

where $\mathbb{C}$ is the right Cauchy deformation tensor.

In this study, the inelastic deformation and breakage of coarse grains are not considered. This simplification is acceptable since the deformation of soil-composing minerals (silicates) is negligible due to their high hardness; however, under large forces or when coarse grains collide with each other at high speeds (such as in high-speed long-runout landslides), fragmentation is expected to occur. In such cases, a fracture model [56] would be necessary.

3.2. SPH discretization

The mass and momentum equation for total Lagrangian formulation can be discretized as [57, 22]

$$\rho_i = \rho_i^0 \frac{1}{\det(\mathbb{F}_i)} \tag{42}$$

$$\frac{\mathrm{d}\mathbf{v}_i}{\mathrm{d}t} = \frac{1}{\rho_i^0} \sum_j \left(\mathbb{P}_i \mathbb{B}_i^{0\mathrm{T}} + \mathbb{P}_j \mathbb{B}_j^{0\mathrm{T}} \right) \nabla_i^0 W_{ij} V_j^0 + \frac{1}{m_i} \mathbf{f}_i^{f \to c} \tag{43}$$

Here, $\nabla_i^0 W_{ij} = \frac{\partial W(|\mathbf{r}_{ij}^0|, h)}{\partial |\mathbf{r}_{ij}^0|} \mathbf{e}_{ij}^0$ denotes the gradient of the kernel function calculated at the initial reference configuration. For coarse grains, the smoothing length is set to $h = 1.15dp$, and the cut-off radius is $2.3dp$. $\mathbf{f}_i^{f \to c}$ will be calculated in Section 4.1. $\mathbb{B}^0$ is the correction matrix, which is applied to satisfy the first-order consistency [58, 59, 60], and is defined as

$$\mathbb{B}_i^0 = \left(\sum_j \left(\boldsymbol{r}_j^0 - \boldsymbol{r}_i^0 \right) \otimes \nabla_i^0 W_{ij} V_j^0 \right)^{-1} \tag{44}$$

The correction matrix is obtained based on the reference configuration, so it only needs to be calculated once. The deformation tensor $\mathbb{F}$ is updated according to its rate of change, which can be discretized as [57]

$$\frac{\mathrm{d}\mathbb{F}_i}{\mathrm{d}t} = \sum_j \left(\boldsymbol{v}_j - \boldsymbol{v}_i \right) \otimes \nabla_i^0 W_{ij} V_j^0 \mathbb{B}_i^0 \tag{45}$$

Refer to reference [61], we apply an artificial stress damping based on the Kelvin-Voigt type damper, to enhance the numerical stability of the original TLSPH method. Firstly, the second Piola-Kirchhoff stress $\mathbb{S}$ is reformulated as

$$\mathbb{S} = \mathbb{S}_S + \mathbb{S}_D \tag{46}$$

where $\mathbb{S}_S$ can be calculated based on the constitutive relation Eq. (40), and the damper $\mathbb{S}_D$ is given by [61]

$$\mathbb{S}_D = \frac{\Pi}{2} \left[\left(\frac{\mathrm{d}\mathbb{F}}{\mathrm{d}t} \right)^T \mathbb{F} + \mathbb{F}^T \left(\frac{\mathrm{d}\mathbb{F}}{\mathrm{d}t} \right) \right] \tag{47}$$

$\Pi = \rho c_0 h/2$ is the artificial viscosity [61]. When two coarse grains collide with each other, the contact force between them are calculated following literatures [62, 63].

When using TLSPH to simulate solids, the issue of hourglass modes [64] can affect computational stability. However, related research [64, 65] indicates that hourglass modes only become pronounced when the material undergoes significant deformation. In this study, the elastic modulus of the coarse grains is relatively high, resulting in minimal deformation; therefore, hourglass modes are not observed. Nevertheless, in cases with larger deformations, it is necessary to apply hourglass control methods [64, 65] to enhance computational stability and accuracy.

4. ULSPH-TLSPH coupling approach

4.1. Coupling force formulation

In this section, we present a general coupled approach for TLSPH and ULSPH to compute the coupling force between coarse grains and fine grains. As mentioned earlier, TLSPH is employed to simulate coarse grains, while ULSPH is used to simulate fine grains. We use superscripts c and f to represent the physical quantities on coarse grains and fine grains, respectively.

When considering the forces exerted by coarse grains on fine grains, i.e., $\mathbf{f}^{c\to f}$, the coarse grains are treated as a solid boundary condition as described in Section 2.4. The force $\mathbf{f}^{c\to f}$ can be expressed by

$$\mathbf{f}_i^{c\to f} = \frac{m_i^f}{\rho_i^f}\sum_j \left[\left(\boldsymbol{\sigma}_i^f + \boldsymbol{\sigma}_j^c\right)\cdot \mathbf{e}_{ij}^{fc} + P_{diss}^{*,fc}\mathbf{n}_j^c\right]\frac{\partial W_{ij}^{fc}}{\partial r_{ij}^{fc}}V_j^f \tag{48}$$

where $\mathbf{n}_j^c$ represents the normal directon of particle j on coarse grains. P_{diss}^* is the dissipation term in the Riemann solution P^* (Eq. (20)). P_{diss}^* is given by

$$P_{diss}^* = \frac{\beta\rho_L c_L\rho_R c_R\left(U_L - U_R\right)}{\rho_L c_L + \rho_R c_R} \tag{49}$$

Here, the superscript f and c in $P_{diss}^{*,fc}$ represents the left and right states are obtained from fine and coarse grains, respectively. When a coarse particle j is in the support domain of a fine particle i, then we take $\boldsymbol{\sigma}_j^c = \boldsymbol{\sigma}_i^f$, as indicated in Section 2.4.

Similarly, the force $\mathbf{f}^{f\to c}$ on coarse particles is given by

$$\mathbf{f}_i^{f\to c} = \frac{m_i^c}{\rho_i^c}\sum_j \left[\left(\boldsymbol{\sigma}_i^c + \boldsymbol{\sigma}_j^f\right)\cdot \mathbf{e}_{ij}^{cf} + P_{diss}^{*,cf}\mathbf{n}_i^c\right]\frac{\partial W_{ij}^{cf}}{\partial r_{ij}^{cf}}V_j^c \tag{50}$$

where the left and right states in $P_{diss}^{*,cf}$ are from coarse and fine grains. If a fine particle j falls within the support domain of a coarse particle i, we set $\boldsymbol{\sigma}_i^c = \boldsymbol{\sigma}_j^f$ [18].

4.2. Time integration

The multiple time-stepping scheme [39] is applied here for the coupled time integration of fine and coarse grains. The time step for fine grains is given by [26, 39]

$$\triangle t^f = CFL^f\frac{h^f}{c_0^f + |\mathbf{v}^f|_{\max}} \tag{51}$$

where $|\mathbf{v}^f|_{\max}$ is the maximum particle velocity, and the Courant-Friedrichs-Lewy (CFL) number for fine particles is set to $CFL^f = 0.4$. The time step for coarse grains is given by [39]

$$\triangle t^c = CFL^c\min\left(\frac{h^c}{c_0^c + |\mathbf{v}^c|_{\max}}, \sqrt{\frac{h^c}{|\frac{\mathrm{d}\mathbf{v}^c}{\mathrm{d}t}|_{\max}}}\right) \tag{52}$$

where $|\frac{\mathrm{d}\mathbf{v}^c}{\mathrm{d}t}|_{\max}$ represents the maximum particle acceleration, and $CFL^c = 0.4$.

Usually, the smaller value between $\triangle t^f$ and $\triangle t^c$ is selected as the time step [66, 31] for both coarse and fine grains.

$$\triangle t = \min\left(\triangle t^f, \triangle t^c\right) \tag{53}$$

However, since the Young's modulus of fine grains, such as soils, is much smaller than that of coarse grains, such as boulders, according to Eq. 22, the sound speed in fine grains is typically much lower than that in coarse grains. As a result, the time step for fine grains is larger than that for coarse grains [39]. Hence, forcing $\triangle t = \min\left(\triangle t^f, \triangle t^c\right)$ would result in a significant waste of unnecessary time in the computation of fine grains.

In this study, the multiple time-stepping method is employed, using separate time steps for fine and coarse grains in their respective calculations. Additionally, within one time step of the fine grains, κ time integrations for the coarse grains are performed, where $\kappa = \lceil \frac{\triangle t^f}{\triangle t^c} \rceil$, and $\lceil \bullet \rceil$ represents the ceiling function which rounds a given number up to the nearest integer. It should be noted that the total duration of κ integrations for coarse grains should be equal to one time step for fine grains.

The position-based Verlet scheme [39] is applied here for the time integration of fine and coarse grains, which can achieve strict momentum conservation in this coupling problems. Fig. 3 depicts the multiple time-stepping method for fine and coarse grains by assuming that $\kappa = 5$. By updating the position twice and the velocity once using the acceleration at the half step, the position-based scheme attains the second-order accuracy [39].

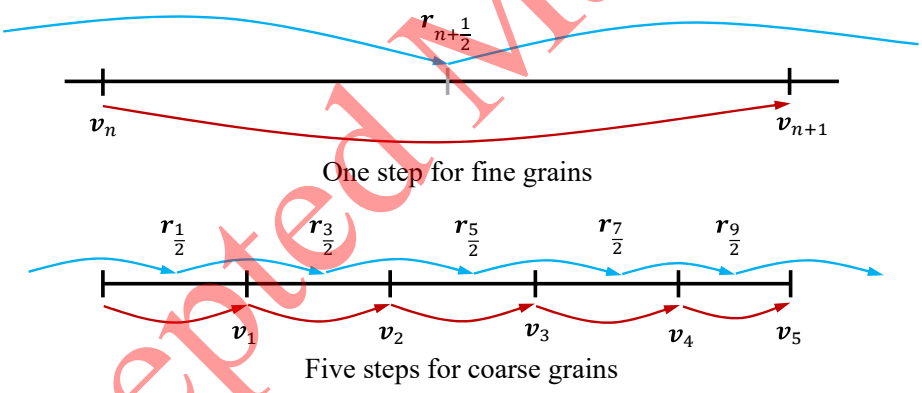

Fig. 3. Illustration of the multiple time-stepping scheme ($\kappa = 5$)

For fine grains, the beginning of the time step is denoted by superscript n, while the midpoint and new time step are denoted by superscripts $n + \frac{1}{2}$ and $n + 1$, respectively. In the Verlet scheme, the particle position and density are initially updated to the midpoint using the following equations

$$\begin{cases} \mathbf{r}^f_{n+\frac{1}{2}} = \mathbf{r}^f_n + \frac{1}{2}\triangle t^f \mathbf{v}^f_n \\ \rho^f_{n+\frac{1}{2}} = \rho^f_n + \frac{1}{2}\triangle t^f \left(\frac{\mathrm{d}\rho}{\mathrm{d}t}\right)^f_n \end{cases} \tag{54}$$

Subsequently, the particle velocity is updated to the new time step once the particle acceleration has been determined.

$$\mathbf{v}^f_{n+1} = \mathbf{v}^f_n + \triangle t^f \frac{\mathrm{d}\mathbf{v}^f}{\mathrm{d}t} \tag{55}$$

Then, the particle position and density are updated to the new time step by

$$\begin{cases} \mathbf{r}^f_{n+1} = \mathbf{r}^f_{n+\frac{1}{2}} + \frac{1}{2}\triangle t^f \mathbf{v}^f_{n+1} \\ \rho^f_{n+1} = \rho^f_{n+\frac{1}{2}} + \frac{1}{2}\triangle t^f \left(\frac{\mathrm{d}\rho}{\mathrm{d}t}\right)^f_{n+1} \end{cases} \tag{56}$$

For coarse grains, the index $\chi = 0, 1, ..., \kappa - 1$ is utilized to represent the integration steps. Employing the position-based Verlet scheme, the deformation tensor, density, and particle position are updated to the midpoint using the following expressions.

$$\begin{cases} \mathbb{F}^c_{\chi+\frac{1}{2}} = \mathbb{F}^c_{\chi} + \frac{1}{2}\triangle t^c \left(\frac{\mathrm{d}\mathbb{F}}{\mathrm{d}t}\right)^c_{\chi} \\ \rho^c_{\chi+\frac{1}{2}} = \rho^c_0 \frac{1}{J} \\ \mathbf{r}^c_{\chi+\frac{1}{2}} = \mathbf{r}^c_{\chi} + \frac{1}{2}\triangle t^c \mathbf{v}^c_{\chi} \end{cases} \tag{57}$$

The velocity is updated by

$$\mathbf{v}^c_{\chi+1} = \mathbf{v}^c_{\chi} + \triangle t^c \frac{\mathrm{d}\mathbf{v}^c}{\mathrm{d}t} \tag{58}$$

Finally, the deformation tensor and the position of coarse grains are updated to the new time step.

$$\begin{cases} \mathbb{F}^c_{\chi+1} = \mathbb{F}^c_{\chi+\frac{1}{2}} + \frac{1}{2}\triangle t^c \left(\frac{\mathrm{d}\mathbb{F}}{\mathrm{d}t}\right)^c_{\chi+1} \\ \rho^c_{\chi+1} = \rho^c_0 \frac{1}{J} \\ \mathbf{r}^c_{\chi+1} = \mathbf{r}^c_{\chi+\frac{1}{2}} + \frac{1}{2}\triangle t^c \mathbf{v}^c_{\chi+1} \end{cases} \tag{59}$$

Prior to starting the next step for fine grains, the time integration of coarse grains, as described by Eqs. (57) to (59), is iterated κ times. Therefore, when calculating the coupling forces between fine and coarse grains, the velocity of coarse grains may display different values, updated after each coarse-grain time step $\triangle t^c$. According to [39], the time-averaged velocity $\overline{\mathbf{v}}^c$ of coarse grains over each time step $\triangle t^f$ is used, which is defined as

$$\overline{\mathbf{v}}^c(n+1) = \frac{1}{\triangle t^f}\left[\mathbf{r}^c_{\chi=\kappa-1}(n+1) - \mathbf{r}^c_{\chi=0}(n+1)\right] \tag{60}$$

It is important to note that the average velocity $\overline{\mathbf{v}}^c$ is only utilized in the computation of the coupling forces between coarse and fine grains. The updates for the coarse grains themselves are based on the velocity $\mathbf{v}^c$ at each time step $\triangle t^c$.

5. Model validation

In this section, we utilize several benchmark cases to validate the effectiveness of our proposed model. Specifically, we perform a comparative analysis, comparing the simulation results with experimental data and SPH results from previous research. This analysis serves to demonstrate the stability and accuracy of our current approach. A fifth-order Wendland kernel [67], as shown

in Eq. (61), is adopted for both fine and coarse grains, with $h = 1.3dp$ for fine grains [34, 20] and $h = 1.15dp$ for coarse grains [22].

$$W(q,h) = \alpha_d \begin{cases} (1-0.5q)^4(2q+1) & 0 \le q \le 2 \\ 0 & q > 2 \end{cases} \tag{61}$$

Here, $q = |\mathbf{r}_{ij}|/h$ represents the ratio of the distance between two particles to the smoothing length h. α_d is the normalization constant, and is equal to $3/(4h)$, $7/(4\pi h^2)$, and $21/(16\pi h^3)$ in one-, two- and three-dimensional space respectively.

5.1. Granular column collapse

First, we verify the motion characteristics of fine grains by employing ULSPH simulation. Granular column collapse is a gravity-driven problem that has been widely studied experimentally [18, 68] and numerically [9, 69, 23, 70]. The experiments conducted by Lube et al. [68] are broadly used to verify SPH simulations [71, 72, 69, 20]. According to previous experimental [68] and numerical [69] studies, the simulation procedure is shown in Fig. 4. A cylindrical granular column, characterized by its height (h_0) and radius (r_0), is released under the influence of self-gravity. The resulting final deposit is measured to determine the run-out distance (r_∞) reached by the column. Referring to [68, 69], the physical parameters are set as follows: density $\rho = 2600$ kg/m^3, Young's module $E = 5.98$ MPa, Poisson's ratio $\nu = 0.3$, friction angle $\phi = 30°$, cohesion $c = 0$ kPa and dilation angle $\psi = 0°$.

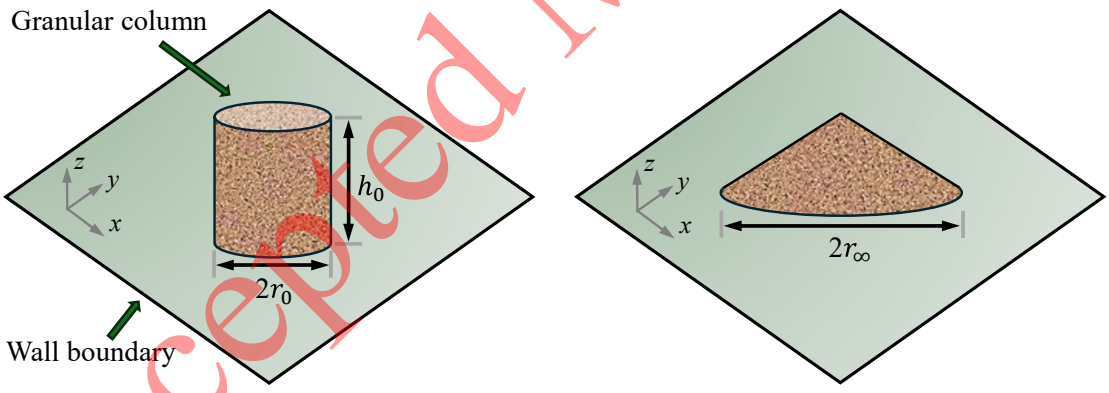

Fig. 4. Simulation of 3D column collapse: (a) initial model setup; (b) final deposit. The diameter and length of the initial granular column are r_0 and h_0 respectively, and the final run-out distance is r_∞.

Fig. 5 displays particle configurations and velocity distributions of a granular column ($r_0 = 0.1$ m and $h_0 = 0.2$ m) at different time instants during the simulation process. To facilitate the visualization of the internal structure, the model has been quartered, retaining only three-quarters of it. It can be observed that the granular column rapidly collapses under the influence of gravity and gradually reaches a stable state. Due to the symmetry of the model, the velocity distribution is also symmetric and uniform. It is worth noting that unlike in Hu et al.'s research [9] where

additional numerical techniques, such as penetration-based particle shifting technique (PPST), are employed to achieve a uniform particle distribution, our model is capable of achieving a highly uniform particle distribution without the need for such corrective methods. This is because we used a low-dissipation Riemann solver [20, 53], which, compared to the artificial viscosity term that can cause excessive numerical dissipation and may affect the physical flow characteristics [51, 53], ensures no or reduced numerical dissipation for expansion and compression waves [53], respectively. The simulation results of column collapse from Nguyen et al. [51] also show that when only the artificial viscosity is applied without other regularization, irregular particle distributions, such as slight depressions and bulges of particles, appear at the base of the slope. Fig. 6 illustrates the distribution of vertical stress and accumulated deviatoric plastic strain in the final deposit. It can be observed that the stress diffuses from the center to the sides of the model, and the stress distribution is smooth. Fig. 6b shows that there is an undisturbed region at the center of the model, which is consistent with previous research [20, 73].

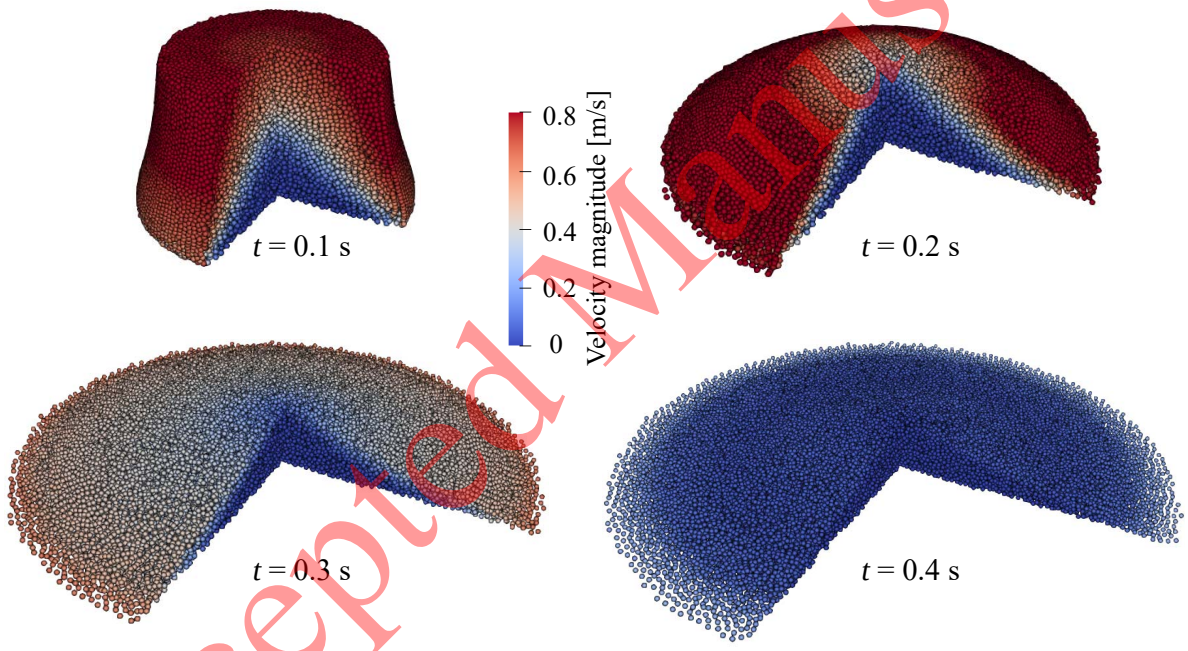

Fig. 5. Snapshots of a granular column at different times during the simulation process. Here, $r_0 = 0.1$ m and $h_0 = 0.2$ m. The initial particle spacing is set to $dp = r_0/20 = 0.005$ m.

Moreover, the convergence and accuracy of the present numerical model is analyzed. We discretize the model using different resolutions ($dp = r_0/10$, $dp = r_0/15$, and $dp = r_0/20$) and investigate the relationship between the run-out distance of the granular column and the initial aspect ratio a ($a = h_0/r_0$). A comparison is made with Lube's empirical equation [68], i.e., $r_\infty = r_0(1 + 1.24a)$ for $a < 1.7$. Firstly, it can be observed that with increasing model resolution, the computed run-out distance r_∞ gradually converge to the reference value. Additionally, the numerical simulation results with $dp = r_0/20$ align with Lube's empirical equation [68], highlighting the accuracy of the model.

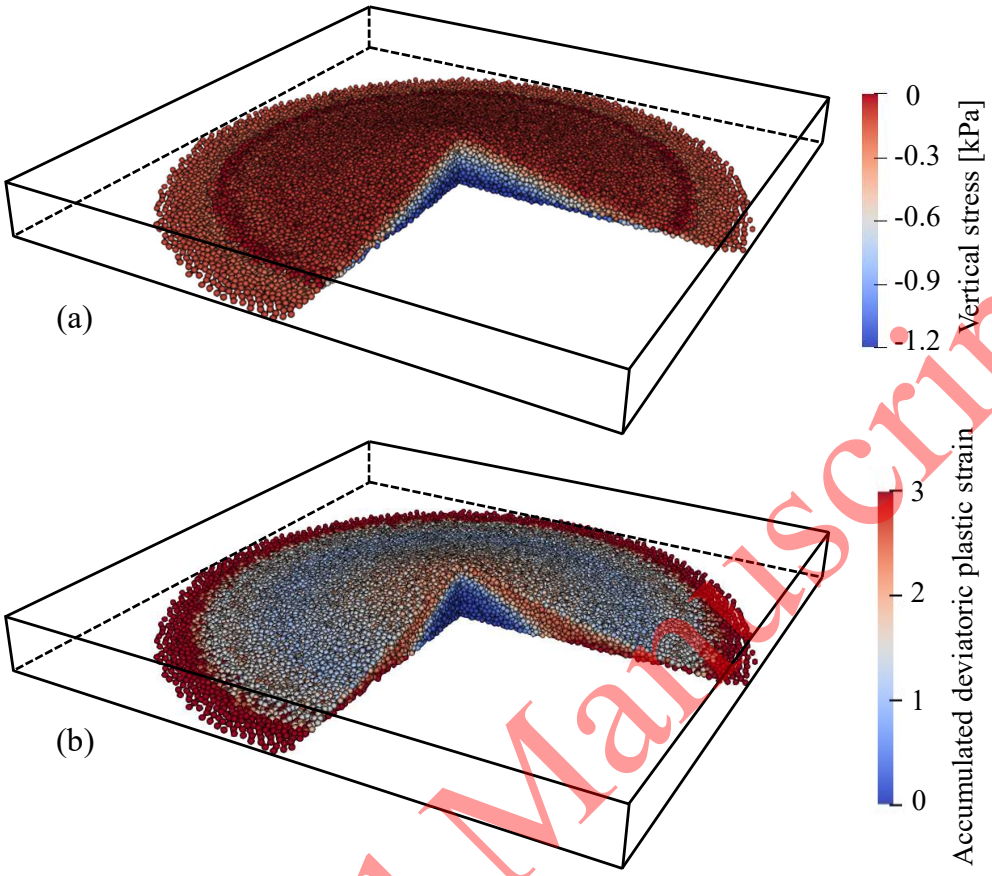

Fig. 6. Illustration of (a) vertical stress and (b) accumulated deviatoric plastic strain for the final deposit. $r_0 = 0.1$ m and $h_0 = 0.2$ m in this case and the initial particle spacing is $dp = r_0/20 = 0.005$ m.

5.2. Low-speed impact craters

In this section, we validate the coupling behavior between ULSPH and TLSPH through the simulation of low-speed impact craters. More specifically, we simulate the formation of craters by dropping balls from a certain height into dry, non-cohesive granular media [74, 75]. The TLSPH method is utilized to simulate the ball as coarse grains, while the granular media is simulated using the ULSPH method to represent fine grains. An initial uniform particle distribution of the ball is achieved by a level-set based pre-processing technique [40].

Uehara et al. [74] and Ambroso et al. [75] have conducted detailed experimental studies on this problem and have summarized the relationship between penetration depth, friction coefficient of the granular media, ball radius, and drop height. Experimental research [74, 75] has also been used by previous scholars to validate their numerical models [9]. Therefore, we will also compare our numerical results with their experimental findings to demonstrate the effectiveness of the proposed model.

The model setup is shown in Fig. 8, a ball with a radius of R_{ball} is dropped from a height H_{ball} above the surface of the granular media, under the influence of gravity. The final penetration depth is D_{ball}, and the total distance traveled by the ball is H_{drop}. Based on the physical tests [74, 75],

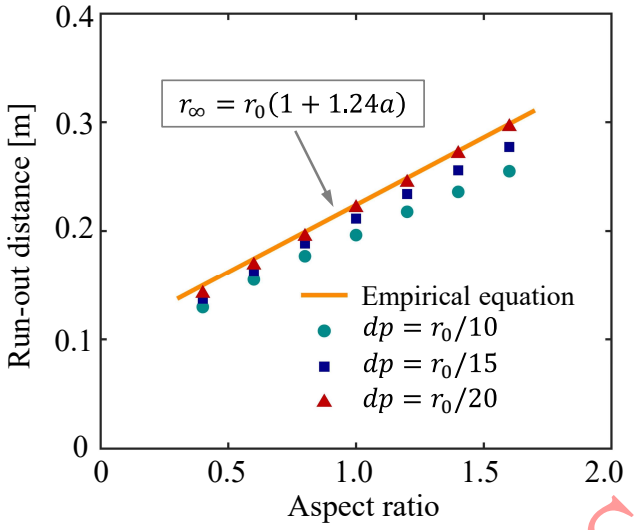

Fig. 7. The influence of aspect ratio a ($a = h_0/r_0$) on the run-out distance: a comparative analysis between our numerical study and Lube's empirical equation [68]. Three different resolutions, i.e., $dp = r_0/10$, $dp = r_0/15$, and $dp = r_0/20$, are considered to verify the convergence and accuracy of the present model.

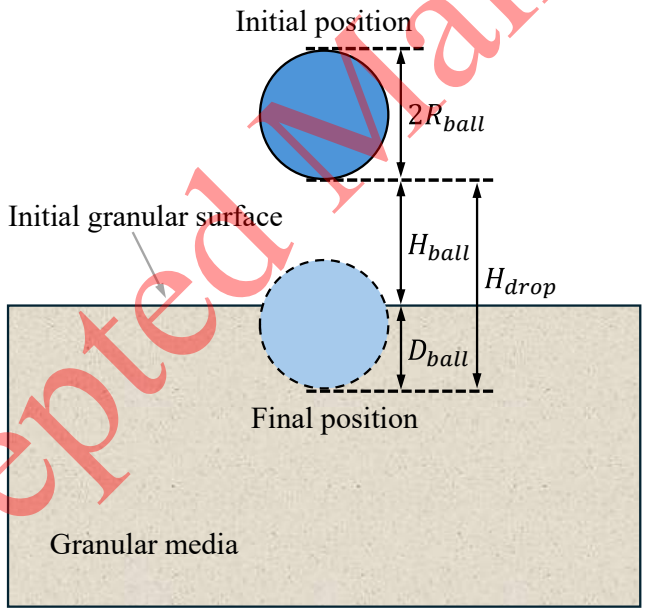

Fig. 8. Model setup for the low-speed impact craters.

the penetration depth (D_{ball}) of the ball follows the empirically derived expression

$$D_{ball} = \frac{0.14}{\mu}\left(\frac{\rho_{ball}}{\rho_{granular}}\right)^{\frac{1}{2}}(2R_{ball})^{\frac{2}{3}}\left(H_{dop}\right)^{\frac{1}{3}} \tag{62}$$

where $\mu = \tan\phi$ is the grain-grain friction coefficient of the granular media [74], and ϕ is the friction angle. ρ_{ball} and $\rho_{granular}$ are the densities of the ball and granular media, respectively.

Referring to [9, 74], the densities of the granular materials and the ball are specified as 1510 kg/m^3 and 2200 kg/m^3, respectively. The Young's moduli for the granular materials and the ball are 2 MPa and 200 MPa, respectively. The Poisson's ratios for the granular materials and the ball are set to 0.3 and 0.25, respectively. The initial particle spacing is set to $dp = 0.002$ m, and The coefficient η in the dissipation limiter is set to $50d$ in this section. According to [9], three different ball heights (0.05 m, 0.1 m and 0.2 m) and two different grain-grain friction coefficients (0.3 and 0.5) are initialized to verify Eq. (62). Unlike past studies [9], where the radius of the ball is fixed at 0.0125 m, we introduced an additional case with a radius of 0.02 m for the purpose of testing. As a result, a total of 12 simulations were conducted, comprising two variations of ball radii, two variations of friction coefficients, and three variations of drop heights.

Fig. 9 shows the snapshots of one simulation with $R_{ball} = 0.02$ m, $H_{ball} = 0.2$ m and $\mu = 0.3$. The top right corner of Fig. 9 shows the ball discretized by SPH particles. The color of the granular material represents the velocity magnitude. Since the ball undergoes free fall motion before coming into contact with the granular material, our focus lies on the interaction process between the ball and granular materials. Hence, we consider $t = 0$ as the instant when the ball just touches the granular material. As the sphere gradually descends, the surrounding particle material is displaced, forming craters. This aligns with our expected results [9], indicating the stability of the algorithm proposed in this paper. Next, we validate the accuracy of the algorithm. Fig. 10 illustrates the variation of penetration depth with ball radius, friction coefficient, and drop height, compared to the empirical equation derived from physical experiments [74, 75]. It can be observed that the simulation results closely align with the experimental findings [74, 75]. The evolution of penetration depth over time is also recorded, as shown in Fig. 11.

5.3. Granular flow impacting blocks

Liu et al. [76] conducted physical experiments to study the impact of granular flow on three wooden blocks and their interactions, which were used to validate numerical models [76, 77]. Building on this, this section will simulate the same scenario and compare the results with both experimental data [76] and previous numerical findings [76, 77]. The setup of the model is shown in Fig. 12. The dimensions of the three blocks are all 0.02 m in length and 0.018 m in height. Consistent with the experimental setup, the block No. 3 is fixed. Therefore, the blocks No. 1 and No. 2 will move under the impact of the granular flow. The material parameters are also taken in accordance with the experimental setup [76]. The initial particle spacing is set to 1.25 mm, and a total of 12800 SPH particles are generated for the granular materials.

Fig. 13 shows the process of granular material gradually collapsing under gravity and impacting the wooden blocks. Snapshots from the experiment [76] are also displayed for comparison. It can be seen that at $t = 0.3$ s, Blocks No. 1 and No. 2 experience significant displacement due to the impact. Block No. 2 falls to the ground around $t = 0.4$ s and remains almost stationary. We measured the angle β (as shown in Fig. 13) between the side of Block No. 2 and the x-axis during this process. The variation of β over time is shown in Fig. 14, which also includes the experimental results [76] and previous numerical results [76, 77]. It can be seen that the initial value of β is 90 degrees. At approximately 0.25 s, when the granular material reaches the blocks, the angle β begins to decrease, reaching about 0 degrees at around 0.45 s. The SPH results presented in this study are in agreement with previous experimental [76] and MPM results [76, 77], indicating that

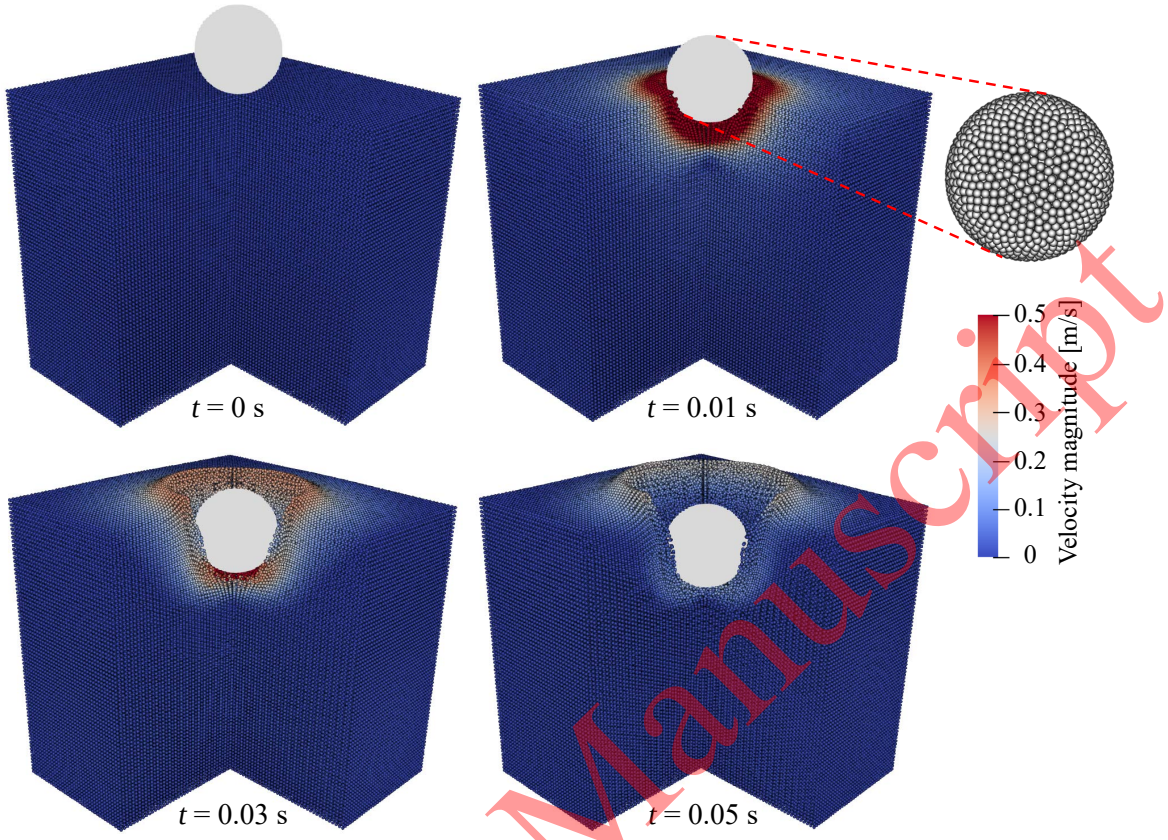

Fig. 9. Snapshots of low-speed impact craters at different times during the simulation. The granular material is colored by velocity magnitude. Here, the ball radius is 0.02 m and the drop height is 0.2 m

the present method can accurately capture the motion behavior of the blocks under the impact of granular flows.

6. Application

We demonstrate the potential engineering applications of the proposed method through two more realistic case studies: soil-rock mixture slopes considering the realistic shape of rock blocks and bouldery debris flows on natural terrain.

6.1. Soil-rock mixture slope

Soil-rock mixtures (SRM), a heterogeneous geomaterial comprising high-strength rock and low-strength soil, is prevalent in natural steep slopes and at the toe of scarps and rock faces in mountainous regions [2, 78]. This unique composition has made SRM a focal point in geotechnical engineering, especially in the analysis of slope instability [15, 79]. In this section, the proposed method is used to simulate the failure of SRM slopes. The soil, represented as fine grains, is simulated using ULSPH, while the rock blocks, represented as coarse grains, are simulated using TLSPH. Following references [15, 80], the model setup is shown in Fig. 15. The slope becomes

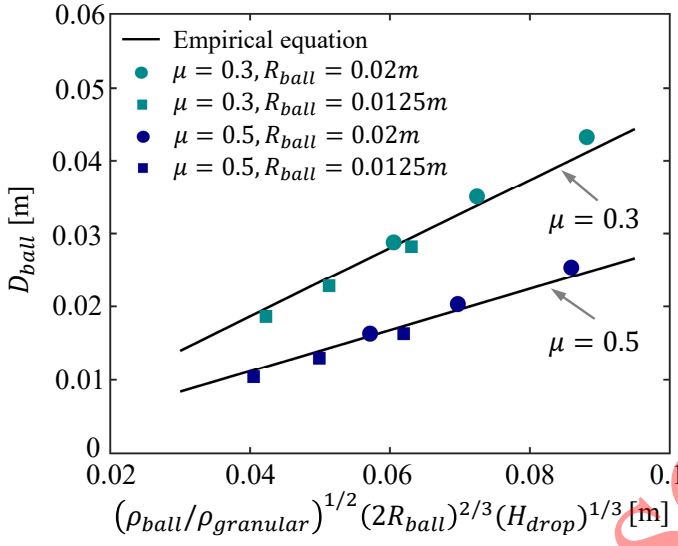

Fig. 10. Penetration depth with different friction coefficients, ball radius, and drop heights. The empirical equation obtained from experimental studies [74, 75] is also presented for comparison.

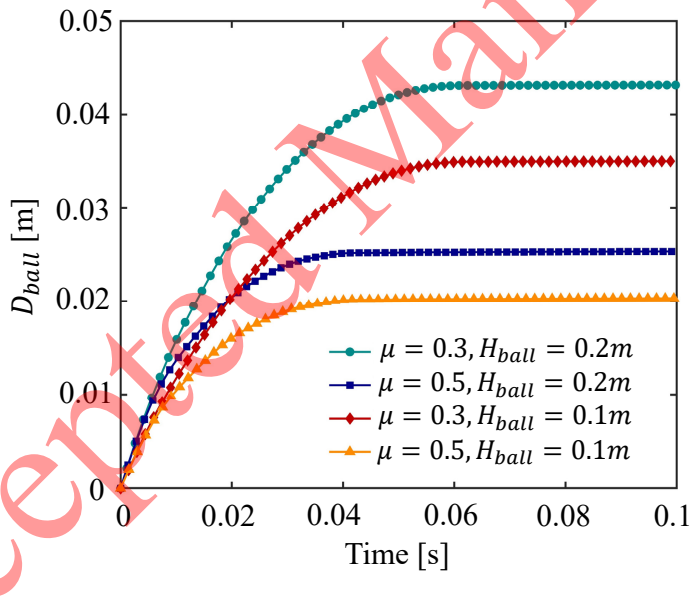

Fig. 11. The variation of penetration depth over time for four different cases with varying friction coefficients and drop heights. The radius of the ball is 0.02 m.

unstable under gravity, moves, and gradually comes to a rest. The run-out distance of the final deposit is measured to conduct a quantitative study. The shapes of the rock particles used in this section are based on real rock blocks photographed and processed through digital image processing [70]. Fig. 16 shows samples of three rock profiles and the discretized rock blocks by using the level-set based pre-processing method [40]. As shown in Table 1, the selection of material parameters for soil and rock blocks follows the literature [15, 80]. The coefficient η in the dissi-

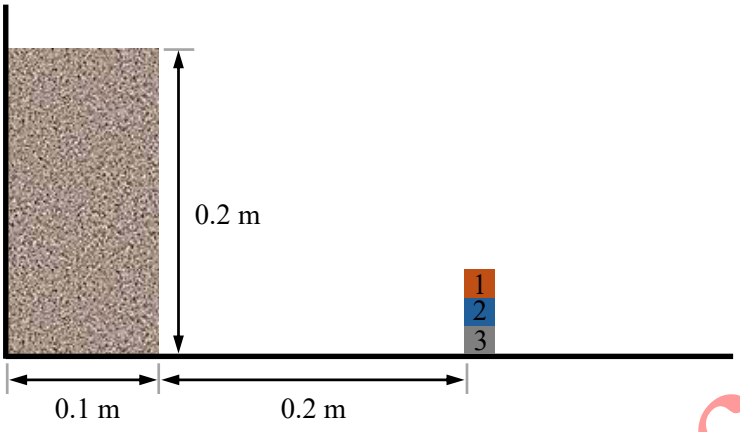

Fig. 12. Model setup of granular collapse with impact on blocks.

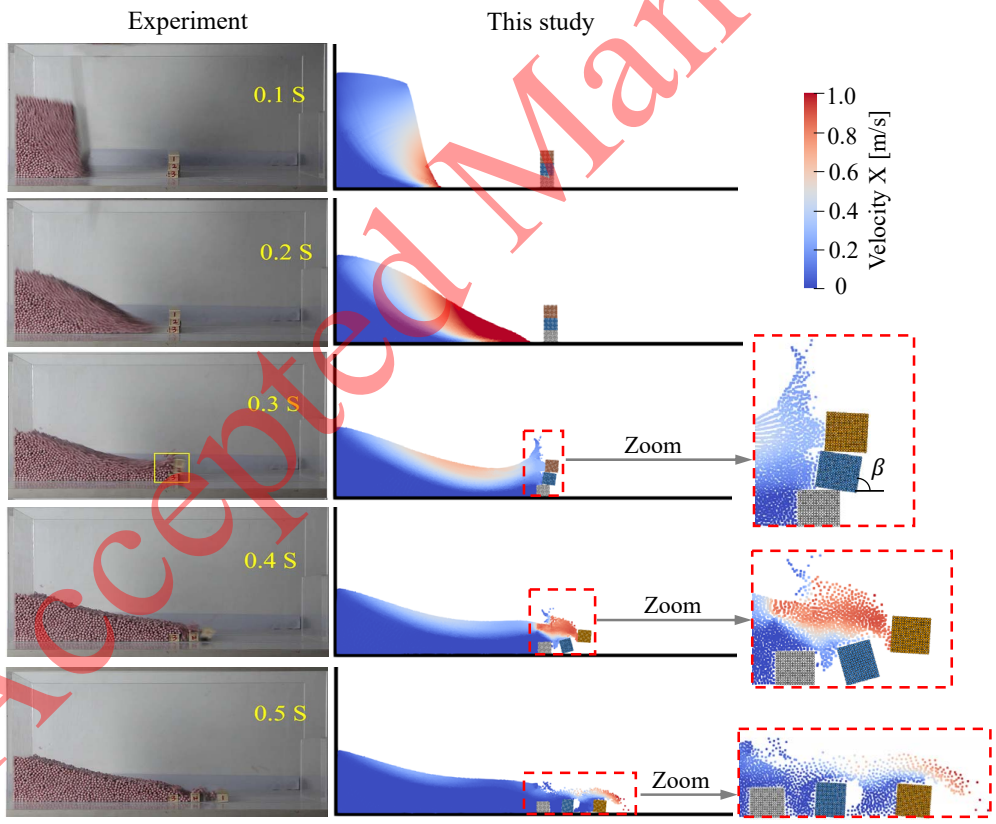

Fig. 13. Snapshots of granular collapse with impact on blocks at different times during the simulation. The first column showcase experimental outcomes [76], while the second column depict the present numerical results at the respective time points. The granular material is colorized by the x-component of velocity.

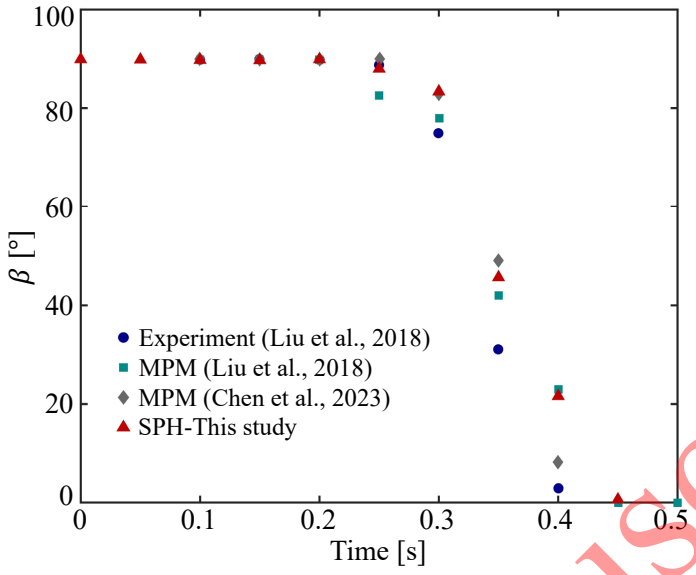

Fig. 14. The temporal evolution of the angle between the left boundary of block No. 2 and the x-axis. The experiment result [76] and MPM simulation results [76, 77] are also shown for comparison.

pation limiter is set to $50d$ and the initial particle spacing is set to 0.5 m. The artificial stress term mentioned in Section 2.3 is applied to in this section to eliminate tensile instability.

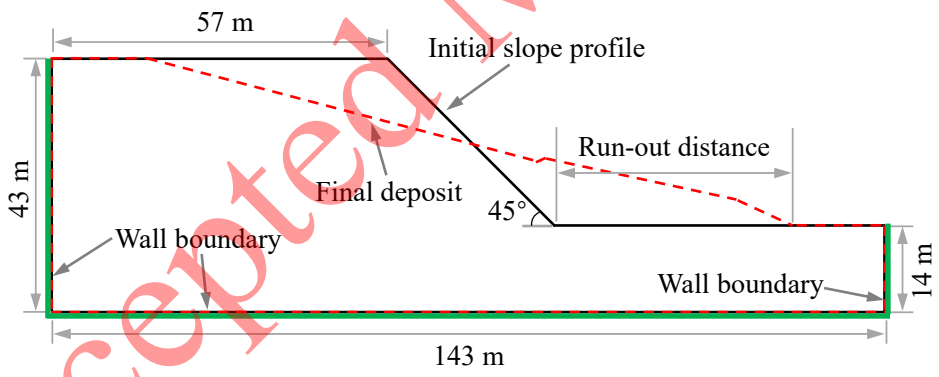

Fig. 15. Model setup of SRM slopes.

First, we investigate the influence of rock block content (RBC) on the run-out distance. By randomly placing rock blocks [2], we constructed slopes with three different rock block contents (10%, 20%, 30%) and compared their results with those of a homogeneous soil slope (RBC = 0%). The RBC is defined as the ratio of the rock area to the total area of rock and soil. To standardize the conditions, the size of the rock blocks is set at 4 m, as recommended within the reasonable range in references [15, 80]. The size D of the rock block is defined as $D = 2\sqrt{A/\pi}$, with A being the area of the rock. Fig. 17 illustrates the dynamic behavior of slopes over time, with varying content of rock blocks. All models have reached a stable state by $t = 10$ s. For homogeneous soil slopes, the sliding band extends from the toe to the top, forming a rotational failure mode. In SRM slopes,

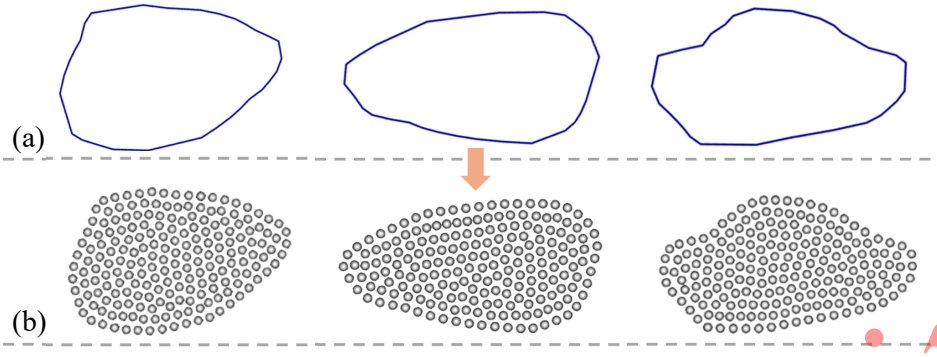

Fig. 16. Illustration of (a) rock block samples and (b) discretization of rock blocks.

Table 1: Material parameters for soils and rock blocks.

Parameter	Soil	Rock
Density (kg/m^3)	2000	2400
Young's modulus (GPa)	3	18
Poisson's ratio	0.35	0.2
Cohesion (kPa)	8.4	-
Friction angle (°)	15	-
Dilation angle (°)	0	-

the development of the plastic zone is usually obstructed by rocks, preventing the formation of a continuous plastic zone from top to bottom as in homogeneous slopes. Instead, it displays a typical pattern of winding around rocks and bifurcating. Hence, SRM slopes exhibit a failure mode with multiple sliding bands due to the combined effect of various plastic zone expansion paths [2]. Among the potential sliding bands that appear in the initial stage, only a few ultimately develop into actual sliding bands.

In SRM slopes, the distribution of rocks is highly random. To reduce this random error, we conducted five parallel tests for each RBC, with different distributions of rocks in each test. Fig. 18 shows the final deposit states for the three rock block contents and the five parallel tests. The run-out distance for each model is measured and plotted with error bars in Fig. 19. The results obtained by MPM [80] and MPM-DEM [15] with different μ_{cf} are also shown for comparison, with μ_{cf} being the friction coefficient between coarse and fine grains. The run-out distance decreases as the rock content increases, which is consistent with previous research findings [15, 80]. Quantitatively, the run-out distances obtained from the current SPH model are close to those from MPM. The MPM-DEM results with $\mu_{cf} = 0$, meaning that the friction between coarse and fine grains is not considered, also fall within the error range of our SPH results. However, the MPM-DEM results show that when $\mu_{cf} = 1$, the run-out distance of the slope can be significantly reduced. Currently, the SPH model does not explicitly account for the friction between coarse and fine grains. In future work, a friction model for interactions between different material types will be implemented within the existing SPH framework.

Fig. 20 demonstrates the effectiveness of artificial stress in eliminating tensile instability. As shown in Fig. 20a, without the application of artificial stress, classic manifestations of tensile instability, such as particle clustering and non-physical fractures, appear on the slope surface.

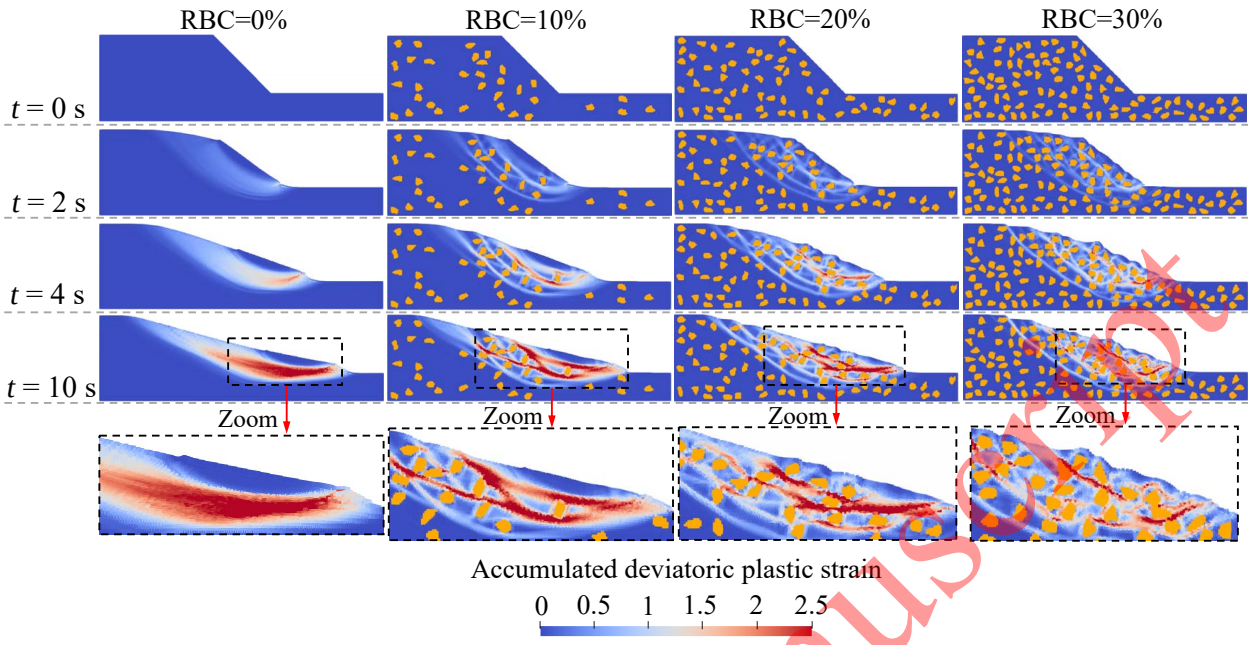

Fig. 17. Snapshots of slope failure under gravity with different rock block contents (0%, 10%, 20%, 30%).

However, after applying artificial stress, as depicted in Fig. 20b, tensile instability is completely eliminated, resulting in a very uniform particle distribution. It is important to note that, although in the cases presented in this section, the presence of tensile instability does not significantly affect the final distribution of the plastic zone and overall deformation, it can lead to severe consequences in other elastic [24] and plastic [34] scenarios reported in the literature.

In the above simulations, a single rock size was used as a controlling variable; however, this single size could not generate a high rock content since there are no smaller rock blocks to fill the voids between larger rock blocks. Here, an SRM slope is generated with rock blocks of different sizes. The constructed slope model, with a RBC of 40%, is shown in Fig. 21a, along with the particle size distribution of coarse grains displayed in the upper right corner. Fig. 21b demonstrates the situation at 10 seconds in the simulation, where three different patterns of plastic zone expansion can be observed: (1) "bypass": the plastic zone circumvents one side of the rock block; (2) "inclusion": the plastic zone closes after circumventing both sides of the rock block; (3) "diversion": the plastic zone remains open after circumventing both sides of the rock block. This is consistent with reports in the literature [2, 78, 81]. Combining Fig. 21 and Fig. 17, it can be observed that an increase in the RBC significantly alters the shape of the failure surface. Specifically, as the RBC increases, the development of the plastic zone transitions from a few thick shear bands to multiple thin and narrow shear bands, resulting in a more fragmented plastic zone. This effect is especially pronounced when the particle size distribution is heterogeneous and there are more smaller-sized rock blocks present, as shown in Fig. 21, which is consistent with the results shown in the reference [2] using finite difference method. This is because the shear bands can only extend through the soil located between the rock blocks. As the number of rock blocks increases, the amount of soil decreases, forcing the shear bands to narrow, and making the plastic zone increasingly frag-

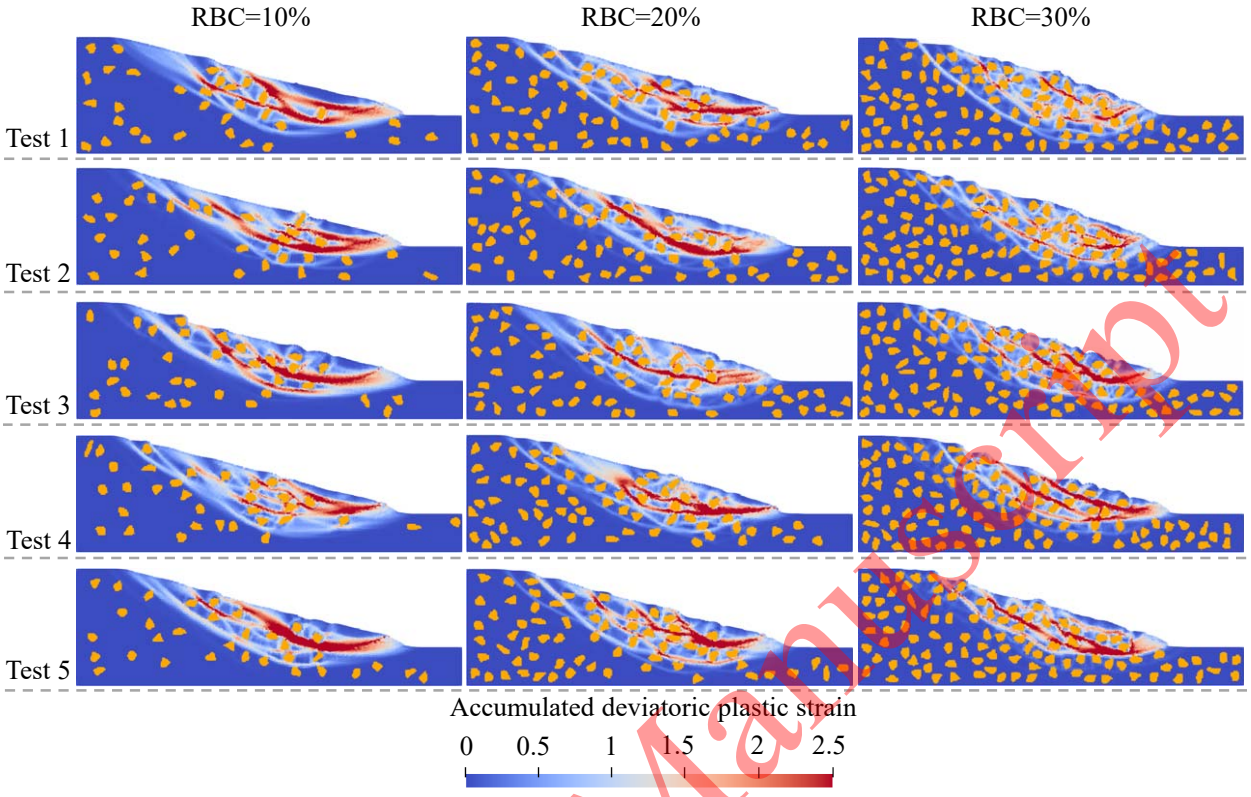

Fig. 18. The final deposits for three sets of RBC (10%, 20%, 30%) and five parallel tests. Each row represents the results of one set of parallel tests.

mented, due to the obstructive and separating effects of the rock blocks on the shear bands. When the particle size distribution is non-uniform, a higher number of small-sized rock blocks under the same RBC further accentuates this effect.

6.2. Bouldery debris flow on natural terrain

This section will further explore the potential of the proposed method in a real debris flow on natural terrain. Initially, a 3D realistic slope surface is created by utilizing UAV-based photogrammetry techniques. For the detailed information of the slope, please refer to Huang et al.'s work [82]. Subsequently, the surface was integrated into SPH and discretized using a level set-based preprocessing method [40]. As depicted in Fig. 22, the slope surface is uneven, with a twisting ravine running down the center of the slope. At the top of the slope, an initial deposit consists of soil (fine grains) and boulders (coarse grains), with the 3D boulder model reconstructed from natural rock fragments using white-light scanning [83, 84]. Some boulders are exposed on the soil surface, especially in areas where the soil layer is relatively thin at the front end of the initial deposit, but more boulders are buried within the soil mass. Fig. 23 showcases the 3D models of various boulder samples alongside the SPH-discretized models. Under the influence of gravity, the initial binary granular mixtures will slide downward to simulate realistic bouldery debris flows. Our aim is to demonstrate that this algorithm can operate reliably under relatively complex conditions involving irregular geometric surfaces and real 3D coarse grain shapes, further validating

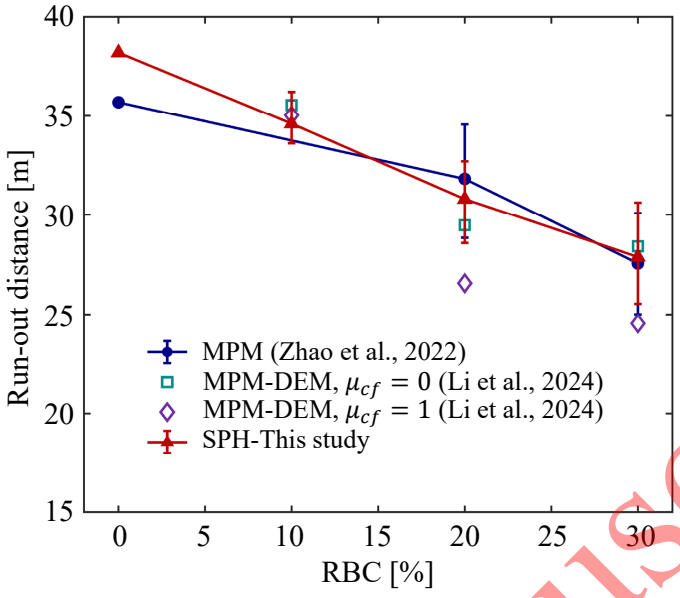

Fig. 19. The relationship between the run-out distance and RBC based on five parallel tests. The results are compared with those obtained by MPM [80] and MPM-DEM [15].

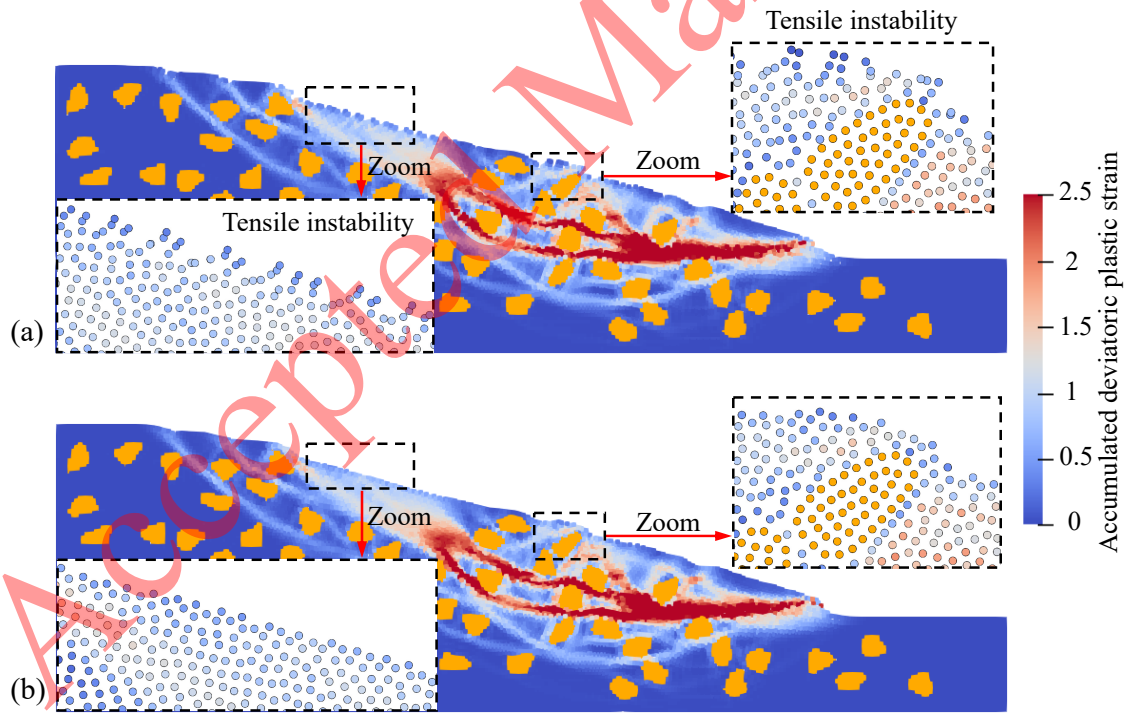

Fig. 20. Illustration of the effect of artificial stress on eliminating tensile instability: (a) without artificial stress; (b) with artificial stress. This is the result for an SRM slope with RBC = 20% at t = 10 s.

its stability and robustness. The material properties for soils and boulders are shown in Table 2

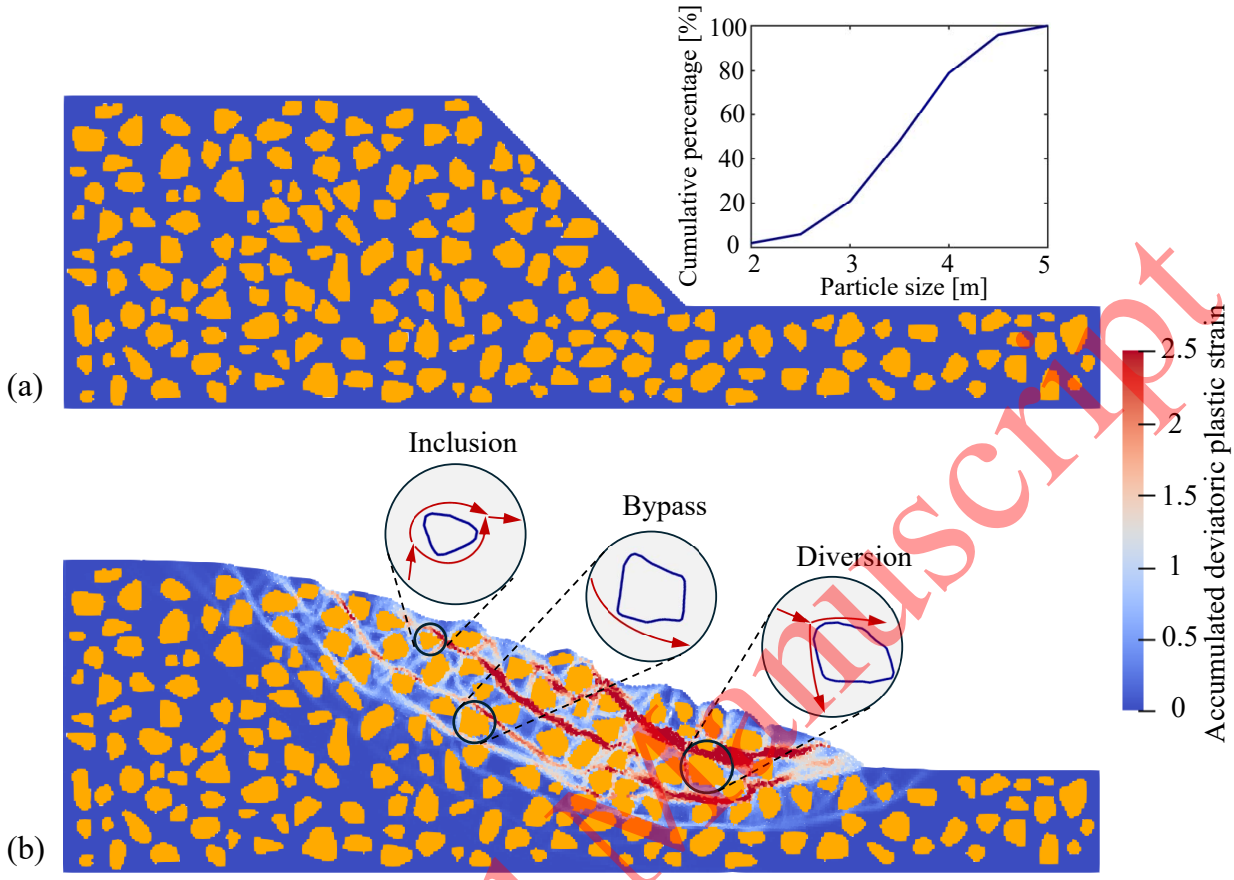

Fig. 21. The simulation of an SRM slope with different rock sizes and RBC = 40% at (a) t = 0 s and (b) t = 10 s. Three different expansion modes of plastic zone can be observed, i.e., "bypass", "inclusion", and "diversion".

[20, 81], and dp is set to 0.25 m.

Fig. 24 shows snapshots of the bouldery debris flow at various stages of the simulation. The images illustrate how soils and boulders move downslope along the valley under the influence of gravity, eventually reaching and accumulating at the base of the slope. During this process, the boulders gradually migrate to the front of the soil mass (Fig. 24c), and in the final deposit (Fig. 24d), many boulders are positioned at the front, exhibiting particle size segregation [85, 86]. This phenomenon can be explained by gravity-driven segregation [87], which is a combined mechanism of gravity-driven kinetic sieving [88] and squeeze expulsion [89]. When materials are transported downslope, the flow behaves like a fluctuating random sieve, statistically favoring the percolation of smaller grains over larger ones under the influence of gravity, as the smaller grains are more likely to occupy the openings that form beneath them [87, 88, 89]. After the grains have vertically segregated into inversely graded layers, with larger grains positioned above finer ones, depth-dependent velocity shear causes preferential transport of the larger grains toward the front [87].

Next, we introduced slit dams along the path of the bouldery debris flow to impede its movement and further test the stability and reliability of the proposed model. As shown in Fig. 25a,

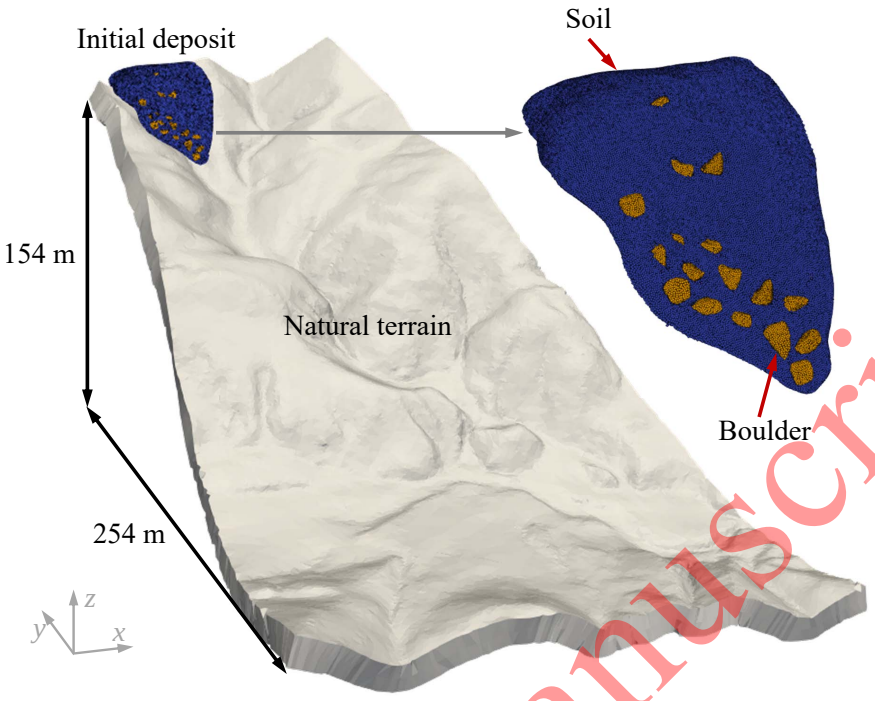

Fig. 22. Model setup of the bouldery debris flow.

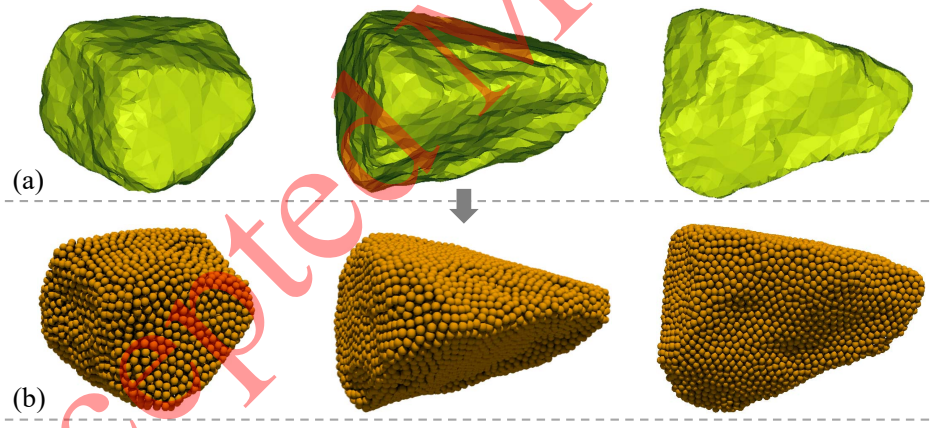

Fig. 23. Illustration of (a) 3D boulder samples and (b) discretization of boulders.

based on the study by Ng et al. [90], the dam heights are set to 0.75-1.5h_f, where h_f is the upstream approach flow depth. In this scenario, despite the uneven surface, the tops of all dams are aligned, resulting in dam heights ranging from 6 to 10 meters. The distance between the centers of two adjacent dams is set at 2 meters, with each dam measuring 1 meter in both length and width. This dam configuration clearly plays a significant role in reducing the impact of the debris flow on downstream areas. As illustrated in Fig. 25b, the slit dams effectively block most of the boulders, although a small number of boulders are diverted to the sides. The movement of the fine fraction is also hindered, with some soils either seeping through the gaps between the dams or overflowing

Table 2: Material parameters for soils and boulders.

Parameter	Soil	Boulder
Density (kg/m^3)	2000	2400
Young's modulus (MPa)	5.98	1000
Poisson's ratio	0.3	0.2
Cohesion (kPa)	0	-
Friction angle (°)	30	-
Dilation angle (°)	0	-

from the top. Ultimately, most of the deposits (soils and boulders) remain on the slope and have not reached the base by t = 40 s, with their velocity significantly reduced.

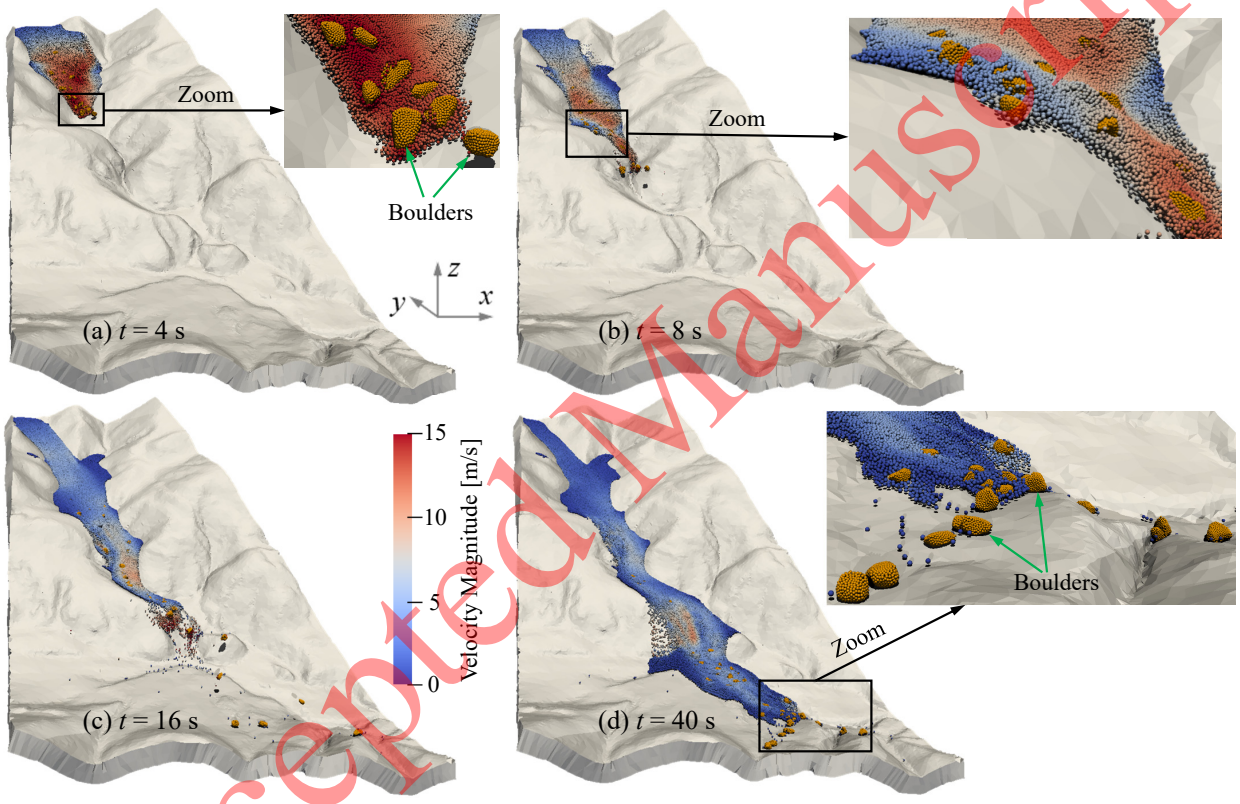

Fig. 24. Bouldery debris flows on natural terrain at different times: (a) t = 4 s; (b) t = 8 s; (c) t = 16 s; (d) t = 40 s.

Fig. 26 quantitatively captures the time evolution of the kinetic energy of the fine and coarse fraction (boulders), both with and without dams. Their kinetic energy rapidly increases to a peak at the start of the simulation, then gradually decreases and stabilizes over time. Notably, before the debris flow reaches the slit dams at around t = 4 s, the changes in kinetic energy are identical regardless of the presence of dams. However, as anticipated, once the debris flow encounters the dams, the kinetic energy of both fractions dissipates more quickly compared to the scenario without dams. It is worth noting that around t = 11 s, a second increase in kinetic energy is observed for the boulders in the no-dam group. This occurs because the boulders gradually move

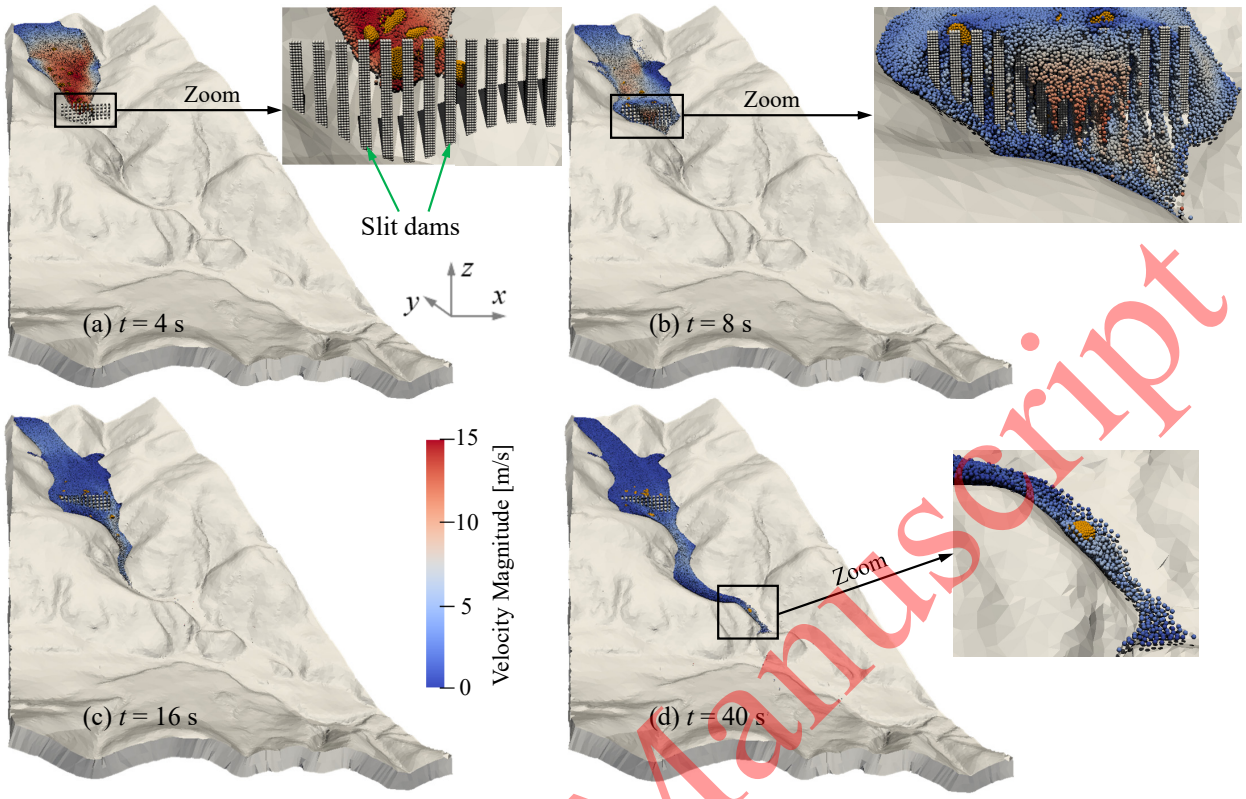

Fig. 25. Bouldery debris flows on natural terrain with slit dams at different times: (a) t = 4 s; (b) t = 8 s; (c) t = 16 s; (d) t = 40 s.

to the front of the soil mass and navigate through terrain depressions into open areas. The absence of additional obstacles leads to a sudden acceleration as gravitational potential energy is converted into kinetic energy. In contrast, the dam group does not exhibit this phenomenon, as most of the boulders are blocked by the dams.

7. Computational efficiency

The present SPH framework is implemented based on the open-source library named SPHinXsys [91], a C++ API for modelling fluids, solids, and fluid-solid interactions with SPH method. In this section, we will delve into the computational efficiency analysis of the proposed ULSPH-TLSPH coupling framework for modelling binary garnular mixtures. All simulations are conducted on a CentOS-8 system with 32 cores. The CPU details are as follows: 64 Intel(R) Xeon(R) Gold 6226R CPUs @ 2.90 GHz.

7.1. Multiple time-stepping scheme versus single time-stepping scheme

The computational efficiency of the multiple time-steeping scheme (Section 4.2) utilized in this study for the coupling problem between coarse and fine grains is analyzed, juxtaposed against the efficiency of the conventional single time-stepping scheme [31, 66].

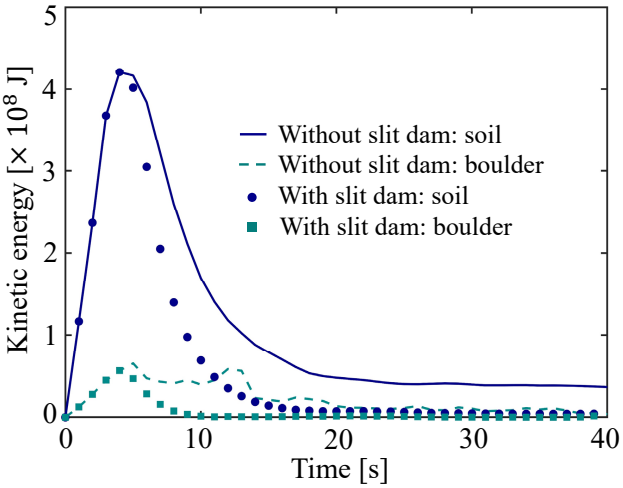

Fig. 26. Time evolution of the kinetic energy of fine and coarse grains with and without slit dams.

Firstly, the calculation efficiency of low-speed impact craters (Section 5.2) is tested with model configurations as shown in Fig. 8. The ball radius is set to 0.02 m and drop height is 0.2 m. Other parameters follow the description in Section 5.2. The simulation ends at physical time $T_P = 0.1$ s. Initial particle spacing dp is set at 4 mm, 2 mm, and 1.5 mm respectively for efficiency testing to reduce random error. The wall clock time spent using the multiple time-stepping scheme (T_W^M) and the single time-stepping method (T_W^S) are shown in Table 3. In each test, the time steps $\triangle t^f$ and $\triangle t^c$ for fine and coarse grains are computed, along with $\kappa = \lceil \frac{\triangle t^f}{\triangle t^c} \rceil$, all detailed in Table 3, facilitating the subsequent analysis of the superior computational efficiency of the multiple time-stepping scheme. The proportion of computational time saved (P_T) by using the multiple time-stepping scheme is defined as

$$P_T = \left(1 - \frac{T_W^M}{T_W^S}\right) \times 100\% \tag{63}$$

The improvement in computational efficiency (I_{CE}) is calculated by

$$I_{CE} = \left(\frac{T_W^S}{T_W^M} - 1\right) \times 100\% \tag{64}$$

As shown in Table 3, compared to the previous method that used the smaller time step between fine and coarse grains, the multiple time-stepping scheme can improve computational efficiency by approximately 600% for this case. This time saving mainly comes from reducing unnecessary iterations for fine grains. Specifically, for the example presented here, $\kappa = 9$, meaning the coarse grains are updated 9 times for every single update of the fine grains; whereas in the previous method, each coarse grain update required a corresponding fine grain update.

Then, the SRM slopes are tested with model configurations as shown in Fig. 17. The simulation ends at physical time $T_P = 10$ s. Initial particle spacing dp is set to 0.7 m, 0.5 m, and 0.3 m, respectively. The wall clock time T_W^M and T_W^S for models with different contents of rock block are shown in Table 4. In this example, the multiple time-stepping approach can improve computa-

Table 3: Computational efficiency test by simulating low-speed impact craters. Here, N_p represents the total number of real particles. T_W^S and T_W^M are wall clock time spent by using the single time-stepping method and the multiple time-stepping scheme, respectively. Physical time $T_P = 0.1$ s for each simulation.

dp (mm)	N_p (k)	$\triangle t^f$ (s)	$\triangle t^c$ (s)	κ	T_W^S (min)	T_W^M (min)	P_T	I_{CE}
4	51.2	$\approx 6.1 \times 10^{-5}$	$\approx 7.4 \times 10^{-6}$	9	9.7	1.5	84.5%	547.7%
2	426.0	$\approx 3.1 \times 10^{-5}$	$\approx 3.7 \times 10^{-6}$	9	138.0	19.9	85.6%	593.5%
1.5	1009.9	$\approx 2.3 \times 10^{-5}$	$\approx 2.8 \times 10^{-6}$	9	439.2	57.6	86.9%	662.5%

Table 4: Computational efficiency test by simulating SRM slopes. Here, N_p represents the total number of real particles. T_W^S and T_W^M are wall clock time spent by using the single time-stepping method and the multiple time-stepping scheme, respectively. Physical time $T_P = 10$ s for each simulation.

RBC	dp (m)	N_p (k)	$\triangle t^f$ (s)	$\triangle t^c$ (s)	κ	T_W^S (min)	T_W^M (min)	P_T	I_{CE}
10%	0.7	8.2	$\approx 2.8 \times 10^{-4}$	$\approx 1.6 \times 10^{-4}$	2	4.3	2.8	34.9%	53.6%
	0.5	16.3	$\approx 2.0 \times 10^{-4}$	$\approx 1.1 \times 10^{-4}$	2	9.3	6.0	35.5%	55.0%
	0.3	45.3	$\approx 1.2 \times 10^{-4}$	$\approx 6.7 \times 10^{-5}$	2	32.8	20.0	39.0%	64.0%
20%	0.7	8.2	$\approx 2.8 \times 10^{-4}$	$\approx 1.6 \times 10^{-4}$	2	4.2	3.1	26.2%	35.5%
	0.5	16.3	$\approx 2.0 \times 10^{-4}$	$\approx 1.1 \times 10^{-4}$	2	8.5	6.0	29.4%	41.4%
	0.3	45.3	$\approx 1.2 \times 10^{-4}$	$\approx 6.7 \times 10^{-5}$	2	31.4	20.1	36.0%	56.2%
30%	0.7	8.2	$\approx 2.8 \times 10^{-4}$	$\approx 1.6 \times 10^{-4}$	2	4.6	3.3	28.3%	39.4%
	0.5	16.3	$\approx 2.0 \times 10^{-4}$	$\approx 1.1 \times 10^{-4}$	2	9.8	6.8	30.6%	44.1%
	0.3	45.3	$\approx 1.2 \times 10^{-4}$	$\approx 6.7 \times 10^{-5}$	2	31.2	20.5	34.3%	52.2%

tional efficiency by approximately 40%-60%. Since κ is only 2 in this case, it does not achieve as much improvement in efficiency as the low-speed impact craters with $\kappa = 9$.

The correlation between κ and I_{CE} is tested by simulating low-speed impact craters, whose setup is simple and thus easily for others to repeat. As shown in Fig. 27, the I_{CE} increases with κ, indicating that the multiple time-stepping scheme becomes more efficient when the ratio of time steps between fine and coarse particles is larger. To aid readers, the wall-clock times for the remaining three cases are provided in Table 5, along with details on the initial particle spacing dp, the number of real particles N_p, and the physical time T_P.

7.2. TLSPH versus ULSPH for modelling coarse grains

This study employs the TLSPH method to simulate coarse grains as elastic materials, offering greater computational efficiency compared to the ULSPH method. This section compares the computational efficiency of the TLSPH and ULSPH methods for simulating elastic solids (coarse grains), followed by an analysis of the efficiency advantages of the present ULSPH-TLSPH framework over a fully ULSPH approach for modeling both coarse and fine grains.

The ULSPH and TLSPH methods are employed to simulate the collision of 2D rubber rings [24] and 3D hollow rubber balls [26], respectively. As is shown in Fig. 28a, two rings, with

Table 5: Computation time for simulating granular column collapse ($h_0 = r_0 = 0.1$ m), granular flow impacting blocks, and bouldery debris flow on natural terrain. Here, T_P denotes the physical time for the simulation and T_W^M represents the wall clock time spent by using the multiple time-stepping scheme.

Case	dp (m)	N_p (k)	T_P (s)	T_W^M (min)
Granular column collapse	0.005	25.1	0.5	2.6
Granular flow impacting blocks	0.00125	13.5	0.5	6.2
Bouldery debris flow on natural terrain	0.25	633.8	40	411.9

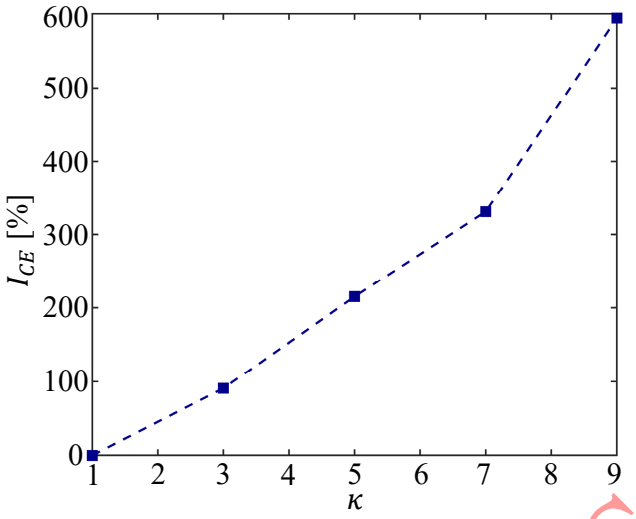

Fig. 27. Correlation between κ and I_{CE} in simulations of low-speed impact craters. Here, the initial particle spacing dp = 2 mm and total number of real particle is 426015.

an inner radius of 0.03 m and an outer radius of 0.04 m, move toward each other. The material parameters are: density ρ^0 = 1200 kg/m^3, Young's modulus E = 10 MPa, and Poisson's ratio ν = 0.4. The initial velocity magnitude $|\mathbf{v}_0| = 0.08c_0$, where c_0 is the sound speed as defined in Eq. (22). The 2D rings are also extended to 3D hollow rubber balls, as shown in Fig. 28b for the middle cross-section, with same material parameters and initial velocity magnitude.

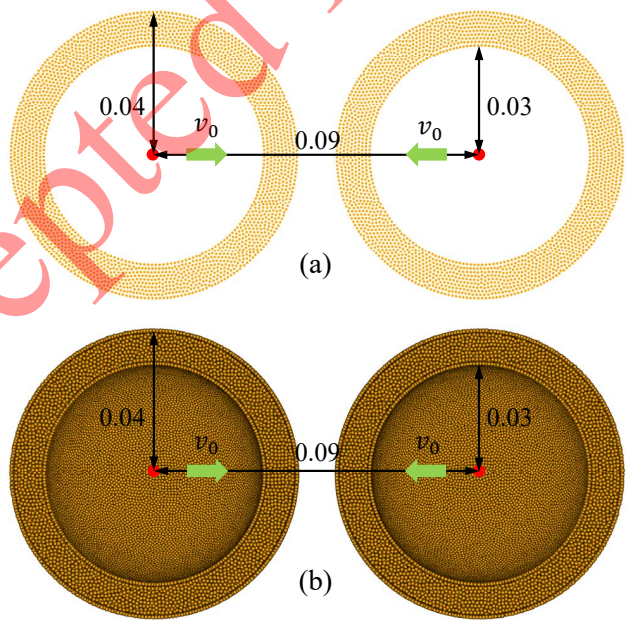

Fig. 28. Model setup for (a) 2D colliding rubber rings and (b) 3D colliding hollow rubber balls (units: m).

Table 6 presents the computation times for the two cases using ULSPH and TLSPH at differ-

Table 6: Comparison of computational efficiency between ULSPH and TLSPH for simulating elastic solids. The physical time for all simulations is 0.01 s.

Case	dp (mm)	N_p (k)	T_W^{UL} (s)	T_W^{TL} (s)	P_T	I_{CE}
2D ring	1	4.4	4.8	2.5	48.0%	92.0%
	0.5	17.6	21.5	8.2	61.9%	162.2%
	0.25	70.4	145.0	48.3	66.7%	200.2%
3D ball	2	38.4	28.4	8.8	69.0%	227.7%
	1.5	91.8	93.9	26.2	72.1%	258.4%
	1	310.0	497.5	132.5	73.4%	275.5%

ent resolutions. It also provides the computational time savings P_T achieved by TLSPH relative to ULSPH, along with the corresponding increase in computational efficiency I_{CE}. It can be observed that the efficiency gain of the TLSPH method for simulating elastic solids increases with the number of SPH particles. In these two test cases, the efficiency improvements in 2D and 3D scenarios reached up to 200.2% and 275.5%, respectively.

Returning to the simulation of binary granular mixtures: suppose the total computation time using the ULSPH-TLSPH coupling framework for a given case is T_W^{UL-TL}, with t^c representing the time spent on computing coarse grains only using TLSPH. Based on the proportion of time saved P_T by TLSPH relative to ULSPH for simulating coarse grains, we can derive the computation time T_W^{UL-UL} required if both coarse and fine grains were simulated entirely using ULSPH.

$$T_W^{UL-UL} = T_W^{UL-TL} - t^c + \frac{t^c}{1-P_T} = T_W^{UL-TL} + \frac{P_T}{1-P_T} t^c \tag{65}$$

For example, for the SRM slope shown in Fig. 21, the total computation time $T_W^{UL-TL} = 282.7$ s, with the coarse grain portion taking $t^c = 109.7$ s. According to Table 6, assuming that the time savings P_T achieved by using TLSPH to simulate coarse grains is 50% relative to ULSPH, the required time when both coarse and fine grains are simulated using ULSPH can be determined to be $T_W^{UL-UL} = 392.4$ s. In other words, compared to simulating both types of grains using ULSPH, the adoption of the ULSPH-TLSPH framework can enhance computational efficiency by 38.8% for this case.

8. Conclusions and outlook

We develop a two-way strong coupling SPH framework to simulate binary granular mixtures. Fine grains are modeled using ULSPH to capture complex granular flow and large deformations, while coarse grains are simulated using TLSPH to enhance computational efficiency. Simulations of three fundamental scenarios, i.e., granular column collapse, low-speed impact craters, and granular flow impacting blocks, demonstrate consistency with experimental and past numerical findings, affirming the stability and accuracy of the proposed approach. Subsequently, simulations are conducted on two realistic cases, namely the soil-rock mixture slope and bouldery debris flow on natural terrain. The analysis of the results is further corroborated by integrating literature analysis, indicating the potential for the proposed method to be applied in other engineering applications. Finally, an analysis of the computational efficiency of the proposed algorithm is performed, demonstrating that the integration of the multiple time-stepping scheme within the

ULSPH-TLSPH coupling framework significantly enhances computational performance, improving efficiency by up to 600%.

The key attributes of the present approach are: (1) its ability to deliver binary mixture simulations of coarse grains and fine grains interacting within a unified SPH framework; (2) capability to simulate complex boundaries and particle shapes; (3) high computational efficiency, facilitating the handling of extensive computational tasks in engineering applications; (4) the coarse grain is simulated by TLSPH as an elastic material, making it deformable rather than rigid. However, at the same time, the method used in this study to calculate the coupling forces between fine grains and coarse grains does not explicitly consider the coefficient of friction between them. Although capturing and computing frictional forces may incur additional computational time, it can be essential in scenarios where friction plays a significant role in the outcomes, even though this aspect is beyond the scope of this paper. Current research [31, 33, 71] exists on computing friction forces between fine grains and rigid bodies using the SPH method, but extending this approach to calculate friction forces with deformable materials has not been documented. Accurately calculating the friction forces of binary mixtures within the SPH framework, while incorporating water to account for the interactions between water, soil, and boulders, will be the focus of our future research.

CRediT authorship contribution statement

Shuaihao Zhang: Conceptualization, Methodology, Investigation, Visualization, Validation, Formal analysis, Writing - original draft, Writing - review & editing. Dong Wu: Methodology, Writing - review & editing. Xiangyu Hu: Methodology, Writing - review & editing. Clarence E. Choi: Investigation, Writing - review & editing. Sérgio D.N. Lourenço: Supervision, Investigation, Writing - review & editing.

Declaration of competing interest

The authors declare that they have no known competing financial interests or personal relationships that could have appeared to influence the work reported in this paper.

Acknowledgements

Sérgio D.N. Lourenço would like to express his gratitude to the Research Grants Council Hong Kong for their sponsorship of this research under a Collaborative Research Fund (C6006-20GF). Dong Wu and Xiangyu Hu would like to express their gratitude to the German Research Foundation (DFG) for their sponsorship of this research under grant number DFG HU1527/12-4. The computations were performed using research computing facilities offered by Information Technology Services, the University of Hong Kong.

References

[1] T. Wang, A. Wautier, J. Zhu, F. Nicot, Stabilizing role of coarse grains in cohesionless overfilled binary mixtures: A DEM investigation, Computers and Geotechnics 162 (2023) 105625.

[2] Z. Lianheng, H. Dongliang, Z. Shuaihao, C. Xiao, L. Yibo, D. Min, A new method for constructing finite difference model of soil-rock mixture slope and its stability analysis, International Journal of Rock Mechanics and Mining Sciences 138 (2021) 104605.
[3] D. Song, C. E. Choi, G. Zhou, J. S. Kwan, H. Sze, Impulse load characteristics of bouldery debris flow impact, Géotechnique Letters 8 (2) (2018) 111–117.
[4] W. Qiu, Y. Li, L. Wen, L. Wang, Z. Xu, Experimental study on the longitudinal evolution of the overtopping breaching of concrete-face sand-gravel dams, Bulletin of Engineering Geology and the Environment 82 (4) (2023) 102.
[5] N. T. Ngo, B. Indraratna, C. Rujikiatkamjorn, Micromechanics-based investigation of fouled ballast using large-scale triaxial tests and discrete element modeling, Journal of Geotechnical and Geoenvironmental Engineering 143 (2) (2017) 04016089.
[6] M. M. Jehring, C. A. Bareither, Tailings composition effects on shear strength behavior of co-mixed mine waste rock and tailings, Acta Geotechnica 11 (2016) 1147–1166.
[7] P. A. Cundall, O. D. Strack, A discrete numerical model for granular assemblies, Geotechnique 29 (1) (1979) 47–65.
[8] J. Gong, J. Liu, L. Cui, Shear behaviors of granular mixtures of gravel-shaped coarse and spherical fine particles investigated via discrete element method, Powder Technology 353 (2019) 178–194.
[9] W. Hu, M. Rakhsha, L. Yang, K. Kamrin, D. Negrut, Modeling granular material dynamics and its two-way coupling with moving solid bodies using a continuum representation and the SPH method, Computer Methods in Applied Mechanics and Engineering 385 (2021) 114022.
[10] Z. Lu, Z. Jin, P. Kotronis, Numerical analysis of slope collapse using SPH and the SIMSAND critical state model, Journal of Rock Mechanics and Geotechnical Engineering 14 (1) (2022) 169–179.
[11] N. Guo, J. Zhao, A coupled FEM/DEM approach for hierarchical multiscale modelling of granular media, International Journal for Numerical Methods in Engineering 99 (11) (2014) 789–818.
[12] Y. Wang, J.-Y. Nie, S. Zhao, H. Wang, A coupled FEM-DEM study on mechanical behaviors of granular soils considering particle breakage, Computers and Geotechnics 160 (2023) 105529.
[13] Y. Jiang, Y. Zhao, C. E. Choi, J. Choo, Hybrid continuum-discrete simulation of granular impact dynamics, Acta Geotechnica 17 (12) (2022) 5597–5612.
[14] S. Ren, P. Zhang, S. Galindo-Torres, A coupled discrete element material point method for fluid-solid-particle interactions with large deformations, Computer Methods in Applied Mechanics and Engineering 395 (2022) 115023.
[15] J. Li, B. Wang, P. Pan, H. Chen, D. Wang, P. Chen, Failure analysis of soil-rock mixture slopes using coupled MPM-DEM method, Computers and Geotechnics 169 (2024) 106226.
[16] R. A. Gingold, J. J. Monaghan, Smoothed particle hydrodynamics: theory and application to non-spherical stars, Monthly notices of the royal astronomical society 181 (3) (1977) 375–389.
[17] L. B. Lucy, A numerical approach to the testing of the fission hypothesis, Astronomical Journal, vol. 82, Dec. 1977, p. 1013-1024. 82 (1977) 1013–1024.
[18] H. H. Bui, R. Fukagawa, K. Sako, S. Ohno, Lagrangian meshfree particles method (SPH) for large deformation and failure flows of geomaterial using elastic–plastic soil constitutive model, International Journal for Numerical and Analytical Methods in Geomechanics 32 (12) (2008) 1537–1570.
[19] Y. Lian, H. H. Bui, G. D. Nguyen, A. Haque, An effective and stabilised (u-pl) SPH framework for large deformation and failure analysis of saturated porous media, Computer Methods in Applied Mechanics and Engineering 408 (2023) 115967.
[20] S. Zhang, C. Zhang, X. Hu, S. D. Lourenço, A Riemann-based SPH method for modelling large deformation of granular materials, Computers and Geotechnics 167 (2024) 106052.
[21] G. Ma, H. H. Bui, Y. Lian, K. M. Tran, G. D. Nguyen, A five-phase approach, SPH framework and applications for predictions of seepage-induced internal erosion and failure in unsaturated/saturated porous media, Computer Methods in Applied Mechanics and Engineering 401 (2022) 115614.
[22] D. Wu, C. Zhang, X. Tang, X. Hu, An essentially non-hourglass formulation for total Lagrangian smoothed particle hydrodynamics, Computer Methods in Applied Mechanics and Engineering 407 (2023) 115915.
[23] A. H. Fávero Neto, R. I. Borja, Continuum hydrodynamics of dry granular flows employing multiplicative

elastoplasticity, Acta Geotechnica 13 (2018) 1027–1040.
[24] J. P. Gray, J. J. Monaghan, R. Swift, SPH elastic dynamics, Computer methods in applied mechanics and engineering 190 (49-50) (2001) 6641–6662.
[25] A. H. Fávero Neto, A. Askarinejad, S. M. Springman, R. I. Borja, Simulation of debris flow on an instrumented test slope using an updated Lagrangian continuum particle method, Acta Geotechnica 15 (2020) 2757–2777.
[26] S. Zhang, S. D. Lourenço, D. Wu, C. Zhang, X. Hu, Essentially non-hourglass SPH elastic dynamics, Journal of Computational Physics (2024) 113072.
[27] J. P. Morris, P. J. Fox, Y. Zhu, Modeling low Reynolds number incompressible flows using SPH, Journal of Computational Physics 136 (1) (1997) 214–226.
[28] J. Cercos-Pita, M. Antuono, A. Colagrossi, A. Souto-Iglesias, SPH energy conservation for fluid-solid interactions, Computer Methods in Applied Mechanics and Engineering 317 (2017) 771–791.
[29] E. Yang, H. H. Bui, G. D. Nguyen, C. E. Choi, C. W. Ng, H. De Sterck, A. Bouazza, Numerical investigation of the mechanism of granular flow impact on rigid control structures, Acta Geotechnica 16 (2021) 2505–2527.
[30] R. Feng, G. Fourtakas, B. D. Rogers, D. Lombardi, A general smoothed particle hydrodynamics (SPH) formulation for coupled liquid flow and solid deformation in porous media, Computer Methods in Applied Mechanics and Engineering 419 (2024) 116581.
[31] L. Zhan, C. Peng, B. Zhang, W. Wu, A SPH framework for dynamic interaction between soil and rigid body system with hybrid contact method, International Journal for Numerical and Analytical Methods in Geomechanics 44 (10) (2020) 1446–1471.
[32] E. M. del Castillo, A. H. Fávero Neto, J. Geng, R. I. Borja, An SPH framework for drained and undrained loading over large deformations, International Journal for Numerical and Analytical Methods in Geomechanics (2024).
[33] H. H. Bui, J. K. Kodikara, A. Bouazza, A. Haque, P. G. Ranjith, A novel computational approach for large deformation and post-failure analyses of segmental retaining wall systems, International Journal for Numerical and Analytical Methods in Geomechanics 38 (13) (2014) 1321–1340.
[34] H. H. Bui, G. D. Nguyen, Smoothed particle hydrodynamics (SPH) and its applications in geomechanics: From solid fracture to granular behaviour and multiphase flows in porous media, Computers and Geotechnics 138 (2021) 104315.
[35] G. Ma, H. H. Bui, Y. Lian, T. V. Nguyen, G. D. Nguyen, Prediction of backward erosion, pipe formation and induced failure using a multi-physics SPH computational framework, International Journal for Numerical and Analytical Methods in Geomechanics (2024).
[36] C. Peng, L. Zhan, W. Wu, B. Zhang, A fully resolved SPH-DEM method for heterogeneous suspensions with arbitrary particle shape, Powder Technology 387 (2021) 509–526.
[37] J. J. Monaghan, Smoothed particle hydrodynamics, In: Annual review of astronomy and astrophysics. Vol. 30 (A93-25826 09-90), p. 543-574. 30 (1992) 543–574.
[38] R. Feng, G. Fourtakas, B. D. Rogers, D. Lombardi, Large deformation analysis of granular materials with stabilized and noise-free stress treatment in smoothed particle hydrodynamics (SPH), Computers and Geotechnics 138 (2021) 104356.
[39] C. Zhang, M. Rezavand, X. Hu, A multi-resolution SPH method for fluid-structure interactions, Journal of Computational Physics 429 (2021) 110028.
[40] Y. Yu, Y. Zhu, C. Zhang, O. J. Haidn, X. Hu, Level-set based pre-processing techniques for particle methods, Computer Physics Communications 289 (2023) 108744.
[41] A. Standard, D2487,", Standard Practice for Classification of Soils for Engineering Purposes (Unified Soil Classification System)", ASTM International, West Conshohocken, PA (2006).
[42] H. Lv, Q. He, X. Chen, P. Han, Numerical simulation of impact crater formation and distribution of high-pressure polymorphs, Acta Astronautica 203 (2023) 169–186.
[43] S. Adami, X. Y. Hu, N. A. Adams, A generalized wall boundary condition for smoothed particle hydrodynamics, Journal of Computational Physics 231 (21) (2012) 7057–7075.
[44] D. C. Drucker, W. Prager, Soil mechanics and plastic analysis or limit design, Quarterly of applied mathematics 10 (2) (1952) 157–165.
[45] R. I. Borja, Plasticity, Springer Berlin Heidelberg 10 (2013) 978–3.

[46] L. R. Alejano, A. Bobet, Drucker–Prager criterion, Rock Mechanics and Rock Engineering 45 (2012) 995–999.
[47] B. Sheikh, T. Qiu, A. Ahmadipur, Comparison of SPH boundary approaches in simulating frictional soil–structure interaction, Acta Geotechnica 16 (2021) 2389–2408.
[48] E. M. del Castillo, A. H. Fávero Neto, R. I. Borja, Fault propagation and surface rupture in geologic materials with a meshfree continuum method, Acta Geotechnica 16 (2021) 2463–2486.
[49] J. K. Dienes, On the analysis of rotation and stress rate in deforming bodies, Acta mechanica 32 (4) (1979) 217–232.
[50] R. I. Borja, C. Tamagnini, Cam-Clay plasticity Part III: Extension of the infinitesimal model to include finite strains, Computer Methods in Applied Mechanics and Engineering 155 (1-2) (1998) 73–95.
[51] C. T. Nguyen, C. T. Nguyen, H. H. Bui, G. D. Nguyen, R. Fukagawa, A new SPH-based approach to simulation of granular flows using viscous damping and stress regularisation, Landslides 14 (2017) 69–81.
[52] J. C. Simo, T. J. Hughes, Computational inelasticity, Vol. 7, Springer Science & Business Media, 2006.
[53] C. Zhang, X. Hu, N. A. Adams, A weakly compressible SPH method based on a low-dissipation Riemann solver, Journal of Computational Physics 335 (2017) 605–620.
[54] J. J. Monaghan, SPH without a tensile instability, Journal of computational physics 159 (2) (2000) 290–311.
[55] J. Bonet, R. D. Wood, Nonlinear continuum mechanics for finite element analysis, Cambridge university press, 1997.
[56] A. de Vaucorbeil, C. R. Hutchinson, A new total-Lagrangian smooth particle hydrodynamics approximation for the simulation of damage and fracture of ductile materials, International Journal for Numerical Methods in Engineering 121 (10) (2020) 2227–2245.
[57] J. J. Monaghan, Smoothed particle hydrodynamics, Reports on Progress in Physics 68 (8) (2005) 1703.
[58] P. Randles, L. D. Libersky, Smoothed particle hydrodynamics: some recent improvements and applications, Computer Methods in Applied Mechanics and Engineering 139 (1-4) (1996) 375–408.
[59] J. Bonet, S. Kulasegaram, A simplified approach to enhance the performance of smooth particle hydrodynamics methods, Applied Mathematics and Computation 126 (2-3) (2002) 133–155.
[60] R. Vignjevic, J. Campbell, Review of development of the smooth particle hydrodynamics (SPH) method, in: Predictive Modeling of Dynamic Processes, Springer, 2009, pp. 367–396.
[61] C. Zhang, Y. Zhu, Y. Yu, D. Wu, M. Rezavand, S. Shao, X. Hu, An artificial damping method for total Lagrangian SPH method with application in biomechanics, Engineering Analysis with Boundary Elements 143 (2022) 1–13.
[62] Y. Zhu, C. Zhang, X. Hu, A dynamic relaxation method with operator splitting and random-choice strategy for SPH, Journal of Computational Physics 458 (2022) 111105.
[63] R. Vignjevic, T. De Vuyst, J. Campbell, C. Source, A frictionless contact algorithm for meshless methods, Computer Modeling in Engineering and Sciences 13 (1) (2006) 35.
[64] G. C. Ganzenmüller, An hourglass control algorithm for lagrangian smooth particle hydrodynamics, Computer Methods in Applied Mechanics and Engineering 286 (2015) 87–106.
[65] D. Wu, X. Tang, S. Zhang, X. Hu, Unified non-hourglass formulation for total lagrangian SPH solid dynamics, Computational Mechanics (2024) 1–33.
[66] L. Zhan, C. Peng, B. Zhang, W. Wu, Three-dimensional modeling of granular flow impact on rigid and deformable structures, Computers and Geotechnics 112 (2019) 257–271.
[67] H. Wendland, Piecewise polynomial, positive definite and compactly supported radial functions of minimal degree, Adv. Comput. Math. 4 (1) (1995) 389–396.
[68] G. Lube, H. E. Huppert, R. S. J. Sparks, M. A. Hallworth, Axisymmetric collapses of granular columns, Journal of Fluid Mechanics 508 (2004) 175–199.
[69] H. Bui, G. D. Nguyen, Numerical predictions of post-flow behaviour of granular materials using an improved SPH model, in: CIGOS 2019, Innovation for Sustainable Infrastructure: Proceedings of the 5th International Conference on Geotechnics, Civil Engineering Works and Structures, Springer, 2020, pp. 895–900.
[70] L. Zhao, S. Zhang, D. Huang, X. Wang, A digitalized 2D particle database for statistical shape analysis and discrete modeling of rock aggregate, Construction and Building Materials 247 (2020) 117906.
[71] Y. Wang, W. Wu, C. Peng, Regularized SPH model for soil–structure interaction with generalized frictional boundary, International Journal for Numerical and Analytical Methods in Geomechanics 47 (10) (2023) 1852–1875.

[72] Z. Lei, B. Wu, S. Wu, Y. Nie, S. Cheng, C. Zhang, A material point-finite element (MPM-FEM) model for simulating three-dimensional soil-structure interactions with the hybrid contact method, Computers and Geotechnics 152 (2022) 105009.
[73] C. Peng, S. Wang, W. Wu, H.-s. Yu, C. Wang, J.-y. Chen, LOQUAT: an open-source GPU-accelerated SPH solver for geotechnical modeling, Acta Geotechnica 14 (2019) 1269–1287.
[74] J. Uehara, M. Ambroso, R. Ojha, D. J. Durian, Low-speed impact craters in loose granular media, Physical Review Letters 90 (19) (2003) 194301.
[75] M. Ambroso, C. Santore, A. Abate, D. J. Durian, Penetration depth for shallow impact cratering, Physical Review E 71 (5) (2005) 051305.
[76] C. Liu, Q. Sun, G. G. Zhou, Coupling of material point method and discrete element method for granular flows impacting simulations, International Journal for Numerical Methods in Engineering 115 (2) (2018) 172–188.
[77] H. Chen, S. Zhao, J. Zhao, X. Zhou, DEM-enriched contact approach for material point method, Computer Methods in Applied Mechanics and Engineering 404 (2023) 115814.
[78] W.-j. Xu, Z.-q. Yue, R.-l. Hu, Study on the mesostructure and mesomechanical characteristics of the soil-rock mixture using digital image processing based finite element method, International Journal of Rock Mechanics and Mining Sciences 45 (5) (2008) 749–762.
[79] L. E. Vallejo, An extension of the particulate model of stability analysis for mudflows, Soils and Foundations 29 (3) (1989) 1–13.
[80] L. Zhao, N. Qiao, D. Huang, S. Zuo, Z. Zhang, Numerical investigation of the failure mechanisms of soil-rock mixture slopes by material point method, Computers and Geotechnics 150 (2022) 104898.
[81] C. Li, G. Chen, L. Guo, J. Gao, X. Peng, P. Yu, Slope stability and post-failure analysis of soil-rock-mixture using the modified 2D DDA-SPH method, International Journal of Rock Mechanics and Mining Sciences 157 (2022) 105170.
[82] G. Huang, G. Lv, S. Zhang, D. Huang, L. Zhao, X. Ni, H. Liu, J. Lv, C. Liu, Numerical analysis of debris flows along the Sichuan-Tibet railway based on an improved 3D sphere DDA model and UAV-based photogrammetry, Engineering Geology 305 (2022) 106722.
[83] S. Zhang, L. Zhao, X. Wang, D. Huang, Quantifying the effects of elongation and flatness on the shear behavior of realistic 3D rock aggregates based on DEM modeling, Advanced Powder Technology 32 (5) (2021) 1318–1332.
[84] L. Zhao, M. Deng, S. Zhang, D. Huang, N. Qiao, J. Gong, Effects of particle shape on triaxial compression behaviours of realistic ballast particles based on MAVL particle shape evaluation system, Granular Matter 25 (1) (2023) 4.
[85] L. Jing, C. Kwok, Y. F. Leung, Micromechanical origin of particle size segregation, Physical review letters 118 (11) (2017) 118001.
[86] C. Johnson, B. Kokelaar, R. M. Iverson, M. Logan, R. LaHusen, J. Gray, Grain-size segregation and levee formation in geophysical mass flows, Journal of Geophysical Research: Earth Surface 117 (F1) (2012).
[87] J. M. N. T. Gray, Particle segregation in dense granular flows, Annual review of fluid mechanics 50 (1) (2018) 407–433.
[88] G. V. Middleton, Experimental studies related to problems of flysh sedimentation., Geol. Assoc. Can. Spec. Paper 7 (1970) 253–272.
[89] S. Savage, C. Lun, Particle size segregation in inclined chute flow of dry cohesionless granular solids, Journal of fluid mechanics 189 (1988) 311–335.
[90] C. W. W. Ng, C. Choi, D. Song, J. Kwan, R. Koo, H. Shiu, K. Ho, Physical modeling of baffles influence on landslide debris mobility: Baffle physical modeling influence on landslide debris mobility, Landslides 12 (2015) 1–18.
[91] C. Zhang, M. Rezavand, Y. Zhu, Y. Yu, D. Wu, W. Zhang, J. Wang, X. Hu, SPHinXsys: An open-source multi-physics and multi-resolution library based on smoothed particle hydrodynamics, Computer Physics Communications 267 (2021) 108066.